The DOI for this manuscript is doi: 10.1175/JPO-D-17-0104.1

The final published version of this manuscript will replace the preliminary version at the above DOI once it is available.

The "bag breakup" spume droplet generation mechanism at high winds. Part I. Spray generation function.

Yu. Troitskaya[1]*, A. Kandaurov[1], O. Ermakova[1], D. Kozlov[1], D. Sergeev[1], S. Zilitinkevich[2,3]

[1] Institute of Applied Physics, Nizhny Novgorod, Russia.

[2] Division of Atmospheric Sciences, University of Helsinki, Finland.

[3] Finnish Meteorological Institute, Helsinki, Finland.

*Corresponding author address: Yuliya Troitskaya, Institute of Applied Physics, 46 Ulyanov str., 603950, Nizhny Novgorod,

E-mail: yuliya@hydro.appl.sci-nnov.ru

ABSTRACT

This paper describes the results of an experimental and theoretical investigation into the mechanisms by which spume droplets are generated by high winds. The experiments were performed in a high-speed wind-wave flume at friction velocities between 0.8 m/s and 1.5 m/s (corresponding to a 10-m wind speed of 18–33 m/s under field conditions). High-speed video of the air–water interface revealed that the main types of spray-generating phenomena near the interface are “bag breakup” (similar to fragmentation of droplets and jets in gaseous flows at moderate Weber numbers), breakage of liquid ligaments near the crests of breaking surface waves, and bursting of large submerged bubbles. Statistical analysis of these phenomena showed that at wind friction velocities exceeding 1.1 m/s (corresponding to a wind speed of approximately 22.5 m/s) the main mechanism responsible for the generation of spume droplets is bag-breakup fragmentation of small-scale disturbances that arise at the air–water interface under the strong wind. Based on the general principles of statistical physics, it was found that the number of bags arising at the water surface per unit area per unit time was dependent on the friction velocity of the wind. The statistics obtained for the bag breakup events and other data available on spray production through this type of fragmentation were employed to construct a spray generation function (SGF) for the bag breakup mechanism. The resultant bag breakup SGF is in reasonable agreement with empirical SFGs obtained under laboratory and field conditions.

1. Introduction

Sea spray is a typical element of the marine atmospheric boundary layer and is of great importance to marine meteorology, atmospheric chemistry, and climate studies. It is considered a crucial factor in the development of hurricanes and severe extratropical storms, which are responsible for the enhancement of energy flux from the ocean to the atmosphere (cf., e.g., Andreas and Emanuel, 2001; Andreas, 2011; Bao et al., 2011; Bianco et al., 2011; Soloviev et al., 2014; Takagaki et al., 2012; Takagaki et al., 2016). According to the concept of re-entrant spray put forward by Andreas and Emanuel (2001), the contribution of spray to the energy flux is dominated by spume droplets: spray mechanically torn off the crests of breaking waves, which rapidly sediments under the effects of gravity before a significant fraction of its volume has had time to evaporate. The spray-mediated momentum flux is also dominated by the spume droplets, which are the main contributors to the volume flux of sea spray (Fairall et al., 1994; Andreas 1998). However, it remains challenging to arrive at estimates for the efficiency of the spray-mediated fluxes because the number and parameters of spume droplets ejected from the water surface into the atmosphere at high winds are uncertain due to both difficulties in taking measurements under storm conditions and uncertainties in the mechanisms of spray generation. As a result, empirical spray generation functions (SGF), which describe the size spectra of spray ejected per unit area per unit time, can differ for the spume droplets by up to six orders of magnitude in different observations (cf., e.g., a compilation of experimental data by Veron (2015) and Andreas (2002)).

Koga (1981) reported the first observations of the process by which spume droplets are generated. This work showed the development of small liquid ligaments, mainly on the crests of breaking waves, that stretch and break, producing one or two droplets. An SGF based on this mechanism was developed by Mueller and Veron (2009). The second mechanism of sea spray production is via the bursting of bubbles formed at the crests of breaking waves, as studied by Blanchard (1963), Spiel (1994a, 1994b, 1995, 1997, 1998), and Lhuissier and Villermaux (2012). Recently, Veron et al. (2012) reported on an alternative mechanism: fragmentation of water surface disturbances in the "bag breakup" regime. On the basis of high-speed video, Troitskaya et al. (2017) classified the spray-generating phenomena, estimated their efficiency and proved that bag-breakup fragmentation is the dominant mechanism of spume droplet production at high winds. In this paper, part I of this study, we construct the SGF for this dominant mechanism and compare it with the available data.

The structure of the paper is as follows. The technical details of the experimental setup and methods of data acquisition and processing are given in Section 2. The classification of phenomena responsible for the generation of spume droplets is described and illustrated in Section 3. Section 3 expands on material briefly presented in Troitskaya et al. (2017) and the Supplement to this paper. The results of statistical analysis of the spray-generating phenomena at different wind speeds are presented in Section 4, with a detailed description of statistics relating to the most efficient bag breakup mechanism. Section 4 also presents possible parameterizations of bag breakup statistics and discusses approaches to applying the data obtained in laboratory experiments to field conditions. The data obtained are employed for constructing an SGF for the bag breakup mechanism in Section 5. In Section 6, the resultant bag breakup SGF is compared with available SGFs that were designed for application under laboratory and field conditions. In Appendix A the dependence of the specific number of "bags" on wind friction velocity u_* is derived from the general principals of statistical physics. Here, it is necessary to quote extensively from the Supplement to Troitskaya et al. (2017) for completeness. Appendices B and C supply the mathematical details of the derivation of the SGF.

2. Experimental setup and methods of measurement

2.1. The experimental setup and parameters of the experiment

Experiments were performed at the wind-wave flume of the Large Thermally Stratified Tank of the Institute of Applied Physics of the Russian Academy of Sciences (IAP RAS). The airflow channel has a cross-section 0.4 m × 0.4 m over the water surface and the length of 10 m. The centerline velocity range is 3–25 m/s. The tank is filled with fresh water, with a temperature ranging from 15 to 20^{o}C. The measured value of the surface tension was $\sigma=(7.0 \pm 0.15)\ 10^{-2}$ N/m. The facility and the parameters of the air flow and surface waves are described in detail in Troitskaya et al. (2012).

To characterize the air flow above the water surface, we use the parameters of the atmospheric turbulent boundary layer: the wind friction velocity, u_*, roughness height, z_0, and 10-m wind speed, defined as follows:

$$U_{10} = \frac{u_*}{\kappa} \ln \frac{H_{10}}{z_0}$$

where κ=0.4 (the von Karman constant) and H_{10}=10 m.

In the wind-wave flume, u_* is in the range 0.2–2 m/s and U_{10} is 7–36 m/s. The dependence of z_0 on u_* in the tank follows the Charnock formula:

$$z_0 = \alpha \frac{u_*^2}{g}, \qquad (1)$$

with the Charnock constant α=0.0057 ± 0.0005 (cf. Fig. 1a).

The wind wave field parameters in the flume were measured by three wire gauges positioned in the corners of an equilateral triangle with 2.5 cm sides; the data sampling rate was 100 Hz. The frequency spectra have sharp peaks depending on u_* and the fetch. The dependency of the peak frequency ω_p on u_* in the working section at a fetch of 6.5 m is plotted in Fig. 1b. The experimental points are best fitted by the power function:

$$\omega_p = \Omega_{u0} u_*^{-\gamma} , \tag{2}$$

where Ω_{u0}=12.4 $m^{1/2}s^{-3/2}$ with the 95% confidence interval between 12.2 $m^{1/2}s^{-3/2}$ and 12.6 $m^{1/2}s^{-3/2}$, and γ=0.5 ± 0.04.

2.2. Optical scheme and experimental techniques for investigating spray-generating phenomena using the shadow method

Using the shadow method for visualization, video of the air–water interface was captured by a NAC Memrecam HX-3 high-speed digital video camera from two angles: a top view of the channel at 6.5 m fetch and a side view at 7.5 m fetch. For the side view, the camera was placed in a waterproof box attached to the side wall of the channel at 7.5 m fetch (the horizontal shadow method, Fig. 2a). The optical axis of the camera lens was located 5 cm above the water surface and was directed horizontally. The distance from the camera to the shooting area was 65 cm. A 300-W LED spotlight was mounted at the side of channel section 8 at a distance of 50 cm from the wall and a height of less than 5 cm from the surface of the water. A diffuser screen was placed on the side wall of the channel opposite the camera. The 85–mm focal length lens provided an image size of 75 × 66 mm (1024 × 904 px, 73 μm pixel size), the recording rate was 10,000 fps, and the exposure time was 50 μs. Detailed side view records of spray-generating phenomena were obtained for wind speeds from 18 m/s to 33 m/s.

To obtain statistics on the spray-generating phenomena, top-view video was filmed using underwater lighting (the vertical shadow method, Fig. 2b). The video was captured through the transparent top wall at 6.5-m fetch. The camera was mounted vertically at a distance of 207 cm from the water surface. The 85–mm focal length lens provided an image size of 147 × 377mm (576 × 1472 px, 256 μm pixel size), the recording rate was 4,500 fps.

3. Classification of phenomena responsible for generation of spume droplets

The combination of the two shooting angles revealed the phenomena responsible for the generation of spume droplets. A brief description and classification of these are given in Troitskaya et al. (2017). This section presents an extended description and new illustrations.

Experiments were performed at airflows with friction velocities from 0.8 m/s to 1.51 m/s corresponding to 10-m wind speeds between 18 m/s and 33 m/s under field conditions according to Foreman and Emeis (2010). Analysis of the images enables us to specify three types of phenomena responsible for the generation of the spume droplets near the wave crest: breakage of liquid ligaments, bursting of large (approximately 1-cm diameter) submerged bubbles, and bag breakup.

3.1. Breakage of liquid ligaments

Fig. 3 illustrates the mechanism by which droplets are generated through breakage of liquid ligaments, as discovered and studied by Koga (1981). Recently, Mueller and Veron (2009) constructed an SGF based on this mechanism. According to Koga (1981), the Kelvin-Helmholtz instability at the air–water boundary leads to the development of liquid ligaments, mainly at the crests of breaking waves, which stretch and then break into droplets. An example of droplet formation by this mechanism under field conditions is shown in Fig. 3e. The details of the structure of the breaking wave crest as shown in insets to Fig. 3e are similar to the structures shown in Fig. 3a–d. Fig. 3b–d confirm that each breakage of a ligament produces a few droplets with diameters of 1–2 mm, which typically fall to the water close to the breaking crest.

3.2. Bursting of large submerged bubbles

Entrainment of air at breaking wave crests leads to the formation of a large number of bubbles, which emerge because of their positive buoyancy and burst into droplets as they reach the water surface (Fig. 4). A detailed model of this phenomenon was recently developed by Lhuissier and Villermaux (2012). The mechanism of the spray production due to bursting of smaller bubbles (less than 10 μm) has been studied by Blanchard (1963) and Spiel (1994a, 1994b, 1995, 1997, 1998). Wu (1981) considered bursting bubbles to be the main source of ocean spray with the radii below 50 μ. According to experiments by Lhuissier and Villermaux (2009, 2012), bursting of a bubble begins with a local reduction of the film thickness and the formation of a hole. The rim bounding the hole moves along the curved surface of the bubble during its expansion. Resulting centrifugal acceleration causes the development of Rayleigh-Taylor instability, accompanied by the formation of ligaments that fragment into droplets. Fig. 4 shows that, in the presence of strong wind and waves at the water surface, the bursting of a submerged bubble touching the water surface occurs as in air and water at rest, as investigated by Lhuissier and Villermaux (2009, 2012).

3.3. Bag breakup.

A sequence of top-view (Fig. 5a) and side-view (Fig. 5b) frames from two different videos illustrates another effective mechanism for generating spume droplets at high wind. It starts with an increase in the small-scale elevation of the surface (Fig. 5a, 0 ms, Fig. 5b, 0 ms), which then transforms into a small liquid “sail”, inflates into a canopy bordered by a thicker rim (the thick rim) (Fig. 5a, 4.7, 8.2 ms, Fig. 5b, 3.4 ms), and finally ruptures to produce spray (Fig. 5a, 10.5 ms, Fig. 5b, 5.6 ms). In some cases, the initial elevated area was transformed into a more complex structure comprising several inflating canopies (Fig. 5c–d). The above-described process by which this occurs is well-known in industrial fluid dynamics as the bag breakup regime of liquid fragmentation in gaseous flows (cf., e.g., Gelfand, 1996). This regime of spume droplet generation at the crests of wind waves was recently observed in a laboratory flume by Veron et al. (2012). Below, we will use the term “bag” to refer to the observed structure.

The process of rupture of the canopy looks similar to the process of bubble bursting investigated by Lhuissier and Villermaux (2009, 2012): it also involves a hole bounded by a rim (the thin rim). A rim moving along the curved film of the canopy during the expansion of the hole leads to the formation of ligaments and drops through the development of Rayleigh-Taylor instability. The thick rim remains after the bubble has burst and then experiences fragmentation into droplets that are large in comparison to those formed at the rupture of the canopy. We emphasize that the distinguishing feature of a bag from a bubble is the presence of two rims limiting the film. As a result, the size distribution of droplets can be expected to show two typical scales.

Fig. 6a–d schematically illustrate the typical stages of fragmentation of the air–water interface in the bag breakup mode, similar to droplets in gaseous flows. Note that research has not yet been able to determine the detailed appearance of the initial disturbance that will be transformed into a bag. In Fig. 6a, it is assumed that the growth of the initial elevation in the water surface is governed by shear flow instability. This assumption is indirectly supported by estimates of the sizes of bags given in Section 4.3. With the increase of the surface elevation, the airflow becomes asymmetrical: the pressure minimum is shifted to the leeward side of the elevated region of water (Fig. 6b), eventually turning it to a liquid sail (Fig. 6c). This process is similar to the transformation of droplets in gaseous flow into a thin disk moving across the flow. The result is the distortion of the shape of the elevated region of water, leading to inflation of the canopy (Fig. 6d), which then raptures (Fig. 6e) and bursts, producing spray.

The statistical analysis below shows that bag breakup appears to be the dominant mechanism of spume droplet generation at high winds.

4. Statistics of local phenomena responsible for generation of spume droplets

4.1. Method and analysis of statistics of spray-generating phenomena

Statistical data for the spray-generating phenomena (breaking ligaments, bursting underwater bubbles, and bag breakup events) was retrieved from the sequence of video frames using software that allows the selection and counting of objects in images semi-automatically (see details in Troitskaya et al., 2017). For the bag breakup events, the software also enables one to obtain the geometrical and kinematic parameters of the objects (cf. Fig. 7), including the initial size, D_1, of the bag, defined as the distance between edge markers in a frame showing the nucleation of the bag; the bag final size, D_2 , defined as the distance between edge markers in a frame showing film puncture; and the bag lifetime from the moment of its nucleation until the moment of film puncture, τ. The velocities of the bag edges and center, u_1, and u_2, were calculated as the distance between, respectively, the midpoints of edge markers or the centers of the canopy on the initial and final frames, divided by τ. Below, we also use the initial and final bag radii, $R_1=D_1/2$ and $R_2=D_2/2$.

Fig. 8a shows the dependence on wind friction velocity, u_*, of the specific number (per unit time per unit area) of spray-generating phenomena obtained using semi-automatic processing. The numbers of processed images are given in Table 1. The number of frames required for the collection of statistics decreased with increasing wind speed, while the number of bags increased. One can see that the specific numbers of local events of any type (ligaments, bursting bubbles, or bags) increase with increasing u_*, with bags showing the greatest growth rate. Note that in the multi-bag regime, each canopy of the complex object was treated in the statistics as one bag. For $u_* < 1.1$ m/s, the numbers of the spray-generating phenomena are approximately equal, beyond which the number of bubble bursts is less than the number of ligaments and bags. For $u_*>1.1$ m/s, the number of bags exceeds the number of ligaments. Given that breaking of one ligament produces only one or two droplets (see Fig. 3) but bag fragmentation produces hundreds of droplets (see Fig. 5) we conclude that, for $u_* >$ 1.1 m/s, bag breakup becomes the dominant mechanism of spume droplet production.

It should be noted that the activation thresholds for the friction velocity were obtained at the laboratory facility. Under field conditions at considerably larger wind fetches and different wind wave regimes, these values may differ. It may be possible to makes estimates of these different values using the approach of Toba and Koga (1986). They suggested parameterizing the strongly nonlinear phenomena in the boundary layers near the air–sea interface using the windsea Reynolds number (this term was suggested later by Toba et al. (2006)):

$$\mathrm{Re}_B = {u_*^2}/{\omega_p \nu}, \qquad (3)$$

where ω_p is the peak frequency in the spectrum of surface wind waves, and ν is the kinematic viscosity of the air. Iida et al. (1992) and Zhao et al. (2006) showed that the parameter Re_B was effective for scaling the spray droplet production rate under both laboratory and field conditions, and Toba and Koga (1986), Zhao et al. (2006) and Toba et al. (2006) successfully used it to scale the wind–sea breaking rate, whitecap coverage and transfer coefficients for momentum and CO_2. Following these studies, we used this parameter for scaling the specific number of the spray-generating phenomena. The peak frequency, ω_p, in the flume was measured directly. At the fetch of the working section, the dependence of peak frequency, ω_p, on u_* is given by Eq. (2).

Fig. 8b plots the specific numbers of bags, bursting bubbles and projections versus the windsea Reynolds number, Re_B. This shows that the threshold for activation of bag breakup, as well as other spray-generating phenomena, is $Re_B \approx 4000$, and that bag breakup becomes the dominant spray-production mechanism for $Re_B > Re_{Bcr} \approx 8000$. Note that, according to Toba and Koga (1986), $Re_{Bcr} \approx 8000$ should be a universal number applicable both under laboratory and field conditions, despite only being retrieved from laboratory data. Given that the gravity wave dispersion relation yields $\omega_p c_p = g$ where c_p is the phase velocity of surface waves with a frequency ω_p, $\mathrm{Re}_B = u_*^3 \big/ g\nu\Omega\sqrt{C_D}$ where $C_D = u_*^2 / U_{10}^2$ is the sea surface drag coefficient and $\Omega = U_{10}/c_p$ is the wave-age parameter. Using the empirical expression of Foreman and Emeis (2010) for $u_*(U_{10})$, $u_* = 0.051U_{10} - 0.14$, for estimating C_D yields the equations for Re_B in terms of U_{10}:

$$Re_B = (0.051U_{10} - 0.14)^2 U_{10} \big/ g\nu\Omega \tag{4}$$

It follows from Eq. (4) that U_{10} decreases with decreasing Ω for a fixed Re_B, and so the threshold wind velocity at which spume spray production will start will decrease with the development of the wave field, which is accompanied by decreasing Ω. This is illustrated in Fig. 8c, where the wind speed is plotted against the wave-age parameter Ω for constant Re_B equal to 4000 and 8000, corresponding to the threshold for activation of the bag breakup mechanism and the condition where bag breakup becomes the dominant mechanism for production of the spume droplets. It follows from Fig. 8c that for Ω between 1 and 3, typical values for open ocean conditions, the bag breakup activation threshold is between 8 m/s and 10 m/s, and at a wind speed between 9.5 m/s and 13 m/s, the mechanism becomes dominant. It is interesting to note that the first range corresponds to number 5 of the Beaufort scale, when, according to the state-of-the-sea scale of Petrsen (1927), “many white horses are formed; chance of some spray.”

It should be emphasized that only droplets with sizes exceeding 10 μm are being discussed here. For smaller droplets, the main generating mechanism is bubble bursting (see, e.g., Wu, 1981), and the contribution of bag-breakup fragmentation is uncertain.

4.2. Statistics of bag breakup events

To describe the statistics on the number of bag breakup events, we use a phenomenological approach based on the Gibbs (1902) method, initially introduced in equilibrium statistical mechanics. The central concept of this method is the canonical ensemble, or the ensemble of states of a large system described in the statistical approach. According to Rumer and Ryvkin (1980), the concept of the Gibbs canonical ensemble allows its universal application to any large system and not just thermodynamic systems consisting of atoms and molecules. Based on this approach, it is possible to derive an expression for the specific number of bag breakup events (see details in the appendix to Troitskaya et al. (2017) and Appendix A) as follows:

$$\langle N \rangle = Q_0 u_*^2 \exp\left(-\frac{U_0^2}{u_*^2} \right), \qquad (5)$$

The constants in Eq. (5), U_0=2 m/s with a 95%-confidence interval between 1.87 m/s and 2.13 m/s, Q_0=9.27·10^2 m^{-4}s with a 95%-confidence interval between 5.91·10^2 m^{-4}s and 1.45·10^3 m^{-4}s, are determined as the best fit to the experimental data shown in Fig. 9a.

Note, that the state of the air–sea system is characterized by one more parameter, the wind fetch. Although the form of the expression for $<N>$ obtained from the general principals of statistical physics remains valid, some changes in the constants are expected with a change in fetch. This should be taken into account when constructing models for field conditions. We here consider a possible parameterization of the specific number of bags with the windsea Reynolds number Re_B (Eq. (3)) introduced by Toba and Koga (1986) and reformulate Eq. (5) accordingly, introducing the dimensionless parameter $V = U_0^2 / \omega_p \nu$. Given that, according to Toba and Koga (1986), the dimensionless V and Q_0, determined by the state of the air–sea interface under the action of wind are functions of Re_B, Eq. (5) yields:

$$\langle N \rangle = Q_0\left(Re_B\right) \frac{Re_B}{V\left(Re_B\right)} exp\left(-\frac{V\left(Re_B\right)}{Re_B} \right).$$

Suppose that $Q_0\left(Re_B\right)$ and $V\left(Re_B\right)$ are the power functions of Re_B, then:

$$\left\langle N\right\rangle = M_0\, Re_B^{\mu_0}\, exp\left(-\frac{M_1}{Re_B^{\mu_1}}\right). \tag{6}$$

To determine constants in Eq. (6) we used the results of Zhao et al. (2006), who showed that the production rate of the spume droplets is proportional to $Re_B^{1.5}$. Given that bag breakup is the dominant mechanism for spume droplet production at Re_B>8000 and assuming that one bag produces on average a certain number of droplets, we can expect that the dependencies of the spume droplet production rate and the specific number of bags on Re_B have the same asymptotics $Re_B^{1.5}$ at large enough Re_B, when the bag breakup spray production mechanism dominates. The best fit to the experimental data in Fig. 9b then gives:

$$\left\langle N\right\rangle = M_0\, Re_B^{3/2}\, exp\left(-\frac{M_1}{Re_B^{3/2}}\right), \tag{7}$$

The best fit to the data in Fig. 9b gives the following constants in Eq.(7): M_0=2.58·10^{-4}m^{-2}s^{-1} with a 95%-confidence interval between 2.22·10^{-4}m^{-2}s^{-1} and 3.00·10^{-4}m^{-2}s^{-1}, M_1=6.93·10^5 with a 95%-confidence interval between 6.22·10^5 and 7.64·10^5, and the relative error in the specific number of bags defined by the 95% confidence interval is approximately 15%.

We also considered another option to translate our laboratory data for field conditions is a simple rescaling of the specific number of bags using the $Re_B^{3/2}$-dependence of the spray production rate. Eq. (3) for Re_B yields, for a certain u_*:

$$\left\langle N\right\rangle_{field} = \left\langle N\right\rangle_{lab}\left(\frac{\omega_{p-lab}}{\omega_{p-field}}\right)^{3/2}.$$

The dispersion relation for the surface gravity waves: $\omega=\sqrt{gk}$ yields $\omega_{p-field}=g/c_p$. This gives

$$\omega_{p-field} = g\Omega/U_{10} = g\Omega\sqrt{C_D}/u_*. \tag{8}$$

Using Eq. (2) for $\omega_{p\text{-}lab}$ and Eq. (8) for $\omega_{p\text{-}field}$ yields the specific number of bags under field conditions:

$$\langle N \rangle_{field} = Q_0 \frac{u_*^2}{U_0^2} \left(\frac{12.4 u_*^{0.5}}{g\Omega\sqrt{C_D}} \right)^{1.5} \exp\left(-\frac{U_0^2}{u_*^2} \right). \tag{9}$$

We compared the values of <N> calculated according to Eqs. (7) and (9), including for hurricane conditions. In accordance with the direct measurements of a wave field in hurricane conditions made by Wright et al. (2001), the wave age parameter, Ω, was taken to be between 2.5 and 3.5. Fig. 9c compares the dependencies of the specific number of bags on wind speed U_{10}, as calculated using Eqs. (7) and (9). For C_D, in both cases we used an approximation of non-monotonous dependence on U_{10} after Holthuijsen et al. (2012), where the latest drop sonde measurements of the drag coefficient were summarized:

$$C_D = \begin{cases} \left(0.057 - 0.48/U_{10}\right)^2 \text{ for } U_{10} < 40\text{m/s} \\ \left(2.37/U_{10} - 0.012\right)^2 \text{ for } U_{10} > 40\text{m/s} \end{cases}$$

A comparison of the curves in Fig. 9c shows that values for <N> when using Eqs. (7) and (9) differ significantly at lower winds, but are very similar at high winds.

It should be emphasized that Eqs. (7) and (9) were obtained on the basis of a limited dataset obtained in a laboratory experiment in a straight channel with a very short wind fetch and, in this regard, should be considered preliminary. The data are not yet sufficient to clearly favor one of the two approaches, and in part II of this study, we will compare the estimates of the exchange coefficients obtained by using each of them. Further refinement of these expressions can be expected as data is accumulated in experiments at large wind fetches, including those with artificial fetch enhancement, as suggested by Takagaki et al. (2017).

4.3. Statistical distributions of the geometrical parameters of bags

Semi-automatic processing of the video allowed us to study the statistical distribution of bag size (radii at nucleation, R_1, and film rupture, R_2), velocity (of edges, u_1, and centers, u_2), and typical lifetime between nucleation and film puncture, τ, for different air flow velocities. Fig. 10a–c show that the probability density of these quantities normalized to the median values can be well-approximated by the gamma distribution:

$$P_n(x) = \frac{n^n}{\Gamma(n)} x^{n-1} e^{-nx} \tag{10}$$

$x = X / \langle X \rangle$ in Eq. (10) represents one of the physical variables R_1, R_2, u_1, u_2 and τ, normalized by its mean value: $\langle R_1 \rangle$, $\langle R_2 \rangle$, $\langle u_1 \rangle$, $\langle u_2 \rangle$, $\langle \tau \rangle$ and $\Gamma(n)$ is Euler's Gamma function. Eq. (10) generalizes the gamma distribution used in Troitskaya et al. (2017) to the case of fractional parameters. For R_1 and R_2, n=7.53, for u_1 and u_2, $n=13.30$, and for τ, $n=3.70$. It is interesting to note that the bag parameters are described by the gamma distribution similarly to completely different objects, for example, droplets produced by fragmentation of ligaments or liquid film (cf. Marmottant and Villermaux, 2004; Lhuissier and Villermaux, 2012).

The dependence of the average values on the friction velocity, u_*, of the air flow is shown in Fig. 11a–c. There is a clear decrease in the size and lifetime of the bags and increase in the velocity of the edges and center with increasing wind speed. The corresponding empirical dependencies can be approximated as follows:

$$\langle R_1 \rangle (u_*) = 5.9 u_*^{-1}, \tag{11}$$

$$\langle R_2 \rangle (u_*) = 9.6 u_*^{-1}, \tag{12}$$

$$\langle u_1 \rangle (u_*) = 1.96 + 1.21\, u_*, \tag{13}$$

$$\langle u_2 \rangle (u_*) = 1.1 + 4.2\, u_*, \tag{14}$$

$$\langle \tau \rangle (u_*) = 7.7\, u_*^{-2}, \tag{15}$$

where u_* is measured in m/s, $\langle R_1 \rangle$ and $\langle R_2 \rangle$ in mm and $\langle \tau \rangle$ in ms.

These dependences of the bag parameters on wind friction velocity can be explained if it is assumed that the water surface perturbations from which they develop arise as a result of the shear instability of the water and air layers near the interface. The thickness of these layers in air and water, δ_a and δ_w, can be estimated as the scales of the buffer layers of turbulent boundary layers, $(20 \div 30)\nu_a / u_*$ and $(20 \div 30)\nu_w / u_* \sqrt{\rho_w / \rho_a}$, respectively (here ν_a and ν_w are the kinematic viscosity coefficients of air and water, and ρ_a and ρ_w are their densities). Note that these quantities are of the same order. The velocity difference in shear layers in air is $\sim (10 \div 12) u_*$ and in the water is $\sim (10 \div 12) u_* \sqrt{\rho_a / \rho_w}$ (see, e.g., Hinze, 1959). The spatial scale of the most unstable disturbances is scaled by the thickness of the shear layer, and then it is $\sim \nu_a / u_*$, in agreement with the dependence of the average bag size on wind friction velocity in Eqs. (11) and (12). Accordingly, the lifetimes of bags of these sizes in a flow with velocity scaled by u_* are proportional to ν_a / u_*^2, in agreement with Eq. (15).

Fig. 11d shows the plane (R_1, R_2), where points correspond to individual bags. These values are proportional, with a correlation coefficient of 0.97. This indicates that the evolution of the bag form is self-similar, i.e., it approximately preserves its form across a range of sizes.

Finally, we can construct the frequency distribution of bag sizes. We present it here as the function of the radius of the bag at the moment of rupture $R = R_2$, which will be used below for constructing an SGF. Combining Eqs. (7) or (9) for the average specific number of bags, $\langle N \rangle$, their size distribution Eq. (10) and the dependence Eq. (12) of the average size $\langle R_2 \rangle (u_*)$ on wind friction velocity gives:

$$F_{bag}(R, u_*) = \frac{\langle N \rangle}{\langle R_2 \rangle (u_*)} \frac{n^n}{\Gamma(n)} \left(\frac{R}{\langle R_2 \rangle (u_*)} \right)^{n-1} e^{-n\left(\frac{R}{\langle R_2 \rangle (u_*)}\right)}, \tag{16}$$

with n=7.53.

5. Construction of a function for spray generation due to the bag breakup mechanism

It is now possible to construct the bag breakup SGF, i.e., the number of spray droplets with radii in the range [r; $r+\Delta r$] generated per unit time per unit area due to the bag breakup mechanism. There are two ways of producing droplets through bag breakup: (i) rupture of the canopy of the inflated bag (Fig. 5a, 10.5 ms and Fig. 5b, 5.6 ms); and (ii) fragmentation of the rim that survives briefly after the rupture of the bag (Fig. 5b, 11.7 ms). Here we first construct the size spectra of droplets produced by each of these two mechanisms.

5.1 The statistical distribution of the canopy droplets

When considering the statistics of the droplets produced by rupture of the bag canopy, we used the results of a detailed study by Lhuissier and Villermaux (2012) concerning a similar mechanism for the generation of spray through the bursting of a submerged bubble touching the surface. Visually, the fragmentation dynamics of the two cases look similar, since they are governed by the same mechanism governed by surface tension. Lhuissier and Villermaux (2012) obtained a size spectrum for droplets (the average number of droplets versus the droplet radius, r) generated through rupture of the bubble cap (the film above the bubble connected to the bulk of the water via a surrounding meniscus) with curvature radius, R, as follows:

$$F_1\left(r,R\right)=\frac{N_{\substack{film\\drops}}\left(R\right)}{\langle r\rangle\left(R\right)}P_m\left(\frac{r}{\langle r\rangle\left(R\right)}\right), \qquad (17)$$

where P_m (x) is the gamma distribution in Eq. (10) with m = 11.

Based on thorough optical measurements, Lhuissier and Villermaux (2012) obtained the dependence of the average diameter, $<d>$, and total number of droplets from the burst of a bubble, $N_{\substack{film\\drops}}(R)$, on R. The power best fit to the experimental data taken from Fig. 20a of Lhuissier and Villermaux (2012) yields the following empirical equation for $<d>$ on R:

$$\langle d\rangle = 0.19L\left(\frac{R^{3/8}h^{5/8}}{L}\right)^{0.8}, \tag{18}$$

Here, h is the thickness of the cup of the bubble at the moment of rupture. According to Lhuissier and Villermaux (2012):

$$h = L\left(\frac{R}{L}\right)^{2}, \tag{19}$$

where L=2 10^4 mm.

The best fit to the experimental data on $N_{\substack{film\\drops}}(R)$, taken from Lhuissier and Villermaux's (2012) Fig. 20b gives:

$$N_{\substack{film\\drops}} = 2.24\cdot 10^{-3}\left(\left(\frac{\rho_w g R^2}{\sigma}\right)\left(\frac{R}{h}\right)^{7/8}\right)^{1.18}. \tag{20}$$

Given that Eqs. (18) and (19) yield the following empirical dependence of the average radius of droplets $<r>=<d>/2$ on the bubble radius:

$$\langle r\rangle(R) = aL\left(\frac{R}{L}\right)^{\alpha};\ a = 0.094;\ \alpha\approx 4/3. \tag{21}$$

and given that Eqs. (19) and (20) yield for the total number of droplets from the burst of a bubble

$$N_{\substack{film\\drops}} = b\left(\frac{R}{L}\right)^{\beta};\ b = 2.24\cdot 10^{-3}\left(\frac{\rho_w g L^2}{\sigma}\right)^{1.18};\ \beta\approx 4/3, \tag{22}$$

for a bag, R is interpreted as its curvature radius at the moment of rupture.

Finally, the total number of droplets with radii in the range [r, $r+\Delta r$] produced by rupture of the bag canopies per unit area per unit time is the convolution of the size spectra of bags (Eq. (16)) with the size spectra of droplets generated due to the rupture of the canopy of the inflated bag (Eq. (17)). Below we will use the term “canopy droplets” to distinguish them from the “canopy droplets” originating from bursting bubbles. The derivation of the equation for the generation function for the canopy droplets, $\frac{dF_c(r)}{dr}$, is presented in Appendix B.

5.2 The statistical distribution of rim droplets.

To describe the size spectrum of droplets resulting from fragmentation of the rim, we consider it as a liquid ligament of a certain thickness prescribed by the radius of the bag, *R*. According to Marmottant and Villermaux (2004), the statistical distribution of droplets produced by fragmentation of such objects follows the gamma distribution (Eq. (10)), with $x=r/r_1$, n=4. Here $r_1=0.4r_0$, where r_0 is defined as the radius of a sphere with a volume equal to the volume of the initial filament (the rim in our case), *V*: $V = 4\pi r_0^3/3$.

Before constructing an SGF for the rim droplets, we need to determine the relationship of the rim volume, *V*, with the measured bag radius, *R*. For this purpose, we use its similarity with the well-known bag breakup regime of secondary fragmentation of droplets in gaseous flows. For this case, Chou and Faeth (1998) showed that the rim volume is equal to 0.56 of the initial volume of a droplet. In the case of bag-breakup fragmentation of the air–water interface, the initial volume of the object that is going to be fragmented is not defined, and we use the following argument. We model the initial shape of a bag as a semi-circular disc with a radius R_1 and thickness h_1. The initial volume of the object is $V_1 = \pi R_1^2 h_1/2$. At the moment of rupture, the shape of a bag with radius R_2 is approximated to a liquid ring (torus) with a thickness h_2, which holds the liquid film. The torus volume is $V = \pi^2 R_2 h_2^2/2$. Based on observations by Chou and Faeth (1998), we assume that the thickness of the rim does not change in the course of its evolution, i.e., $h_1=h_2=H$. We also suppose that the ratio of the rim volume, *V*, to the initial liquid volume, V_1, remains as found by Chou and Faeth

(1998) for the bag breakup regime of the secondary fragmentation of droplets, i.e. V=0.56V_1. We then have $0.56\pi R_1^2 H/2 = \pi^2 R_2 H^2/2$ and $H = 0.56 R_1^2/\left(\pi R_2\right)$.

Given the strong correlation between R_1 and R_2 seen in Fig. 11d (the coefficient of determination is above 0.95), we assume a linear relationship between R_1 and R_2. The linear best fit line shown in Fig. 11d gives $R_2 \approx 1.66 R_1$. Finally, $H = 0.56 R_2/\left(1.66^2 \pi\right) = 0.065 R_2$, and the rim volume is $V = \pi^2 R_2 H^2/2 = 0.021 R_2^3$. The radius of an equivalent sphere is $r_0 = \sqrt[3]{3V/4\pi} = 0.17 R_2$ and the scale in the gamma distribution for the "rim" droplets according to Marmottant and Villermaux (2004), r_1=0.4r_0=γ R_2 where γ=0.068.

The average number of rim droplets from one bag, $N_{\substack{rim\\drops}}$, can be found as the ratio of the rim volume, V, to the average volume of a drop, <V>, resulting from its fragmentation. Given that the size statistics of the rim droplets is described by the gamma distribution with the parameter 4, we have:

$$\left\langle V \right\rangle = \frac{4\pi}{3} r_1^3 \int_0^\infty x^3 \frac{4^4}{3!} x^3 e^{-4x} dx = \frac{15}{8}\frac{4\pi}{3} r_1^3 .$$

For r_1=0.4r_0, we have $N_{\substack{rim\\drops}} = V/\left\langle V \right\rangle = 8.3$.

Finally, the size spectrum of droplets (average number of droplets over the whole range of radii, r) generated through fragmentation of the rims is as follows:

$$F_2\left(r,R\right) = \frac{N_{\substack{rim\\drops}}}{\gamma R} P_k\left(\frac{r}{\gamma R}\right), \tag{23}$$

where P_k (x) is the gamma distribution (Eq. (10)) with k=4, γ=0.068, $N_{\substack{rim\\drops}} = 8.3$. Here and below we use the notation R instead of R_2.

The total number of rim droplets with radii in the range [r,r+Δr] produced by bags per unit area per unit time is the convolution of the size spectra of bags (Eq. (16)) with the size spectra of droplets generated due to the fragmentation of the rim (Eq. (23)). The expression for the generation function for the rim droplets is derived in Appendix C.

The complete bag breakup SGF is the sum of the contributions of the canopy and rim droplets given in Appendices B and C (Eqs. (B6) and (C5), respectively)

$$\frac{dF(r,u_*)}{dr} = \langle N \rangle \left(\frac{3.3\cdot 10^{-9}}{L} \left(\frac{\rho_w g L^2}{\sigma} \right)^{1.18} \left(\frac{r}{\theta} \right)^{7.3} e^{-5.2\sinh\left(\frac{3}{7}\ln\frac{r}{\theta}\right)} + \frac{1.5\cdot 10^{-4} N_{\substack{rim \\ drops}}}{\Theta} \left(\frac{r}{\Theta} \right)^{4.5} e^{-3.94\sinh\left(\frac{1}{2}\ln\frac{r}{\Theta}\right)} \right). \tag{24}$$

In Eq. (24), $\langle N \rangle$ is defined by Eqs. (5) and (7). Expressions for θ and Θ are derived in Appendices B and C, respectively: $\theta = 0.001\left(\langle R_2 \rangle (u_*)\right)^{4/3} L^{-1/3}$, $\Theta = 0.0021\langle R_2 \rangle (u_*)$, where $\langle R_2 \rangle (u_*)$ is expressed by Eq. (12) and L=20 m (cf. Lhuissier and Villermaux, 2012). The uncertainty of the SGF given by Eq. (24) as well as the specific number of bags, $\langle N \rangle$, is about 15% with a 95% confidence interval.

6. Properties of the spray generation function for bag breakup and comparison with laboratory and field data

The SGF defined by Eq. (24) is shown in Fig. 12a. It has two clear peaks, corresponding to canopy droplets with average radii of approximately 100 µm and giant rim droplets with average radii of approximately 1 mm; this is shown directly in Fig. 12b, which plots $\frac{dF_{rim}(r,u_*)}{dr}$ and $\frac{dF_{film}(r,u_*)}{dr}$ separately. The rim-droplet peak at r =500–1000 µm is the distinctive feature of the bag breakup spray generation mechanism. Giant droplets torn off the wave crests have also been observed in laboratory experiments reproducing hurricane conditions (Veron et al., 2012; Ortiz-Suslow et al., 2016; Iida et al., 1992, Fairall et al., 2009). Note that although the number of giant rim droplets is small, we can expect that they will significantly support the spray volume flux. This is confirmed by a strongly enhanced peak in the SGF as a volume flux at sizes of about 1000 μm, corresponding to the rim droplets (cf. Fig. 12c). It should also be noted that the maxima in size spectra of the droplets change with wind speed, similarly to Mueller and Veron (2009), because the average size of the bag, $\langle R_2 \rangle (u_*)$, which in turn scales both canopy and rim droplets (θ, Eq. (B7) and Θ, Eq.(C6)), depends on u_*.

We compare in Fig. 13 the bag breakup SGF (Eq. (24)) with available experimental SGFs derived from laboratory data by Iida et al. (1992), Fairall et al., 2009, Veron et al. (2012) and Ortiz-Suslow et al. (2016). We used the wind friction velocity as the control parameter since this allows direct comparison with earlier data. The data points of Fairall et al. (2009), Veron et al. (2012) and Ortiz-Suslow et al. (2016), reproduced in Fig. 13, confirm that they observed the presence of the giant droplets with sizes of hundreds of micrometers in the air flow, in agreement with the bag breakup SGF. The earlier SGF suggested by Iida et al. (1992) shows a very slow decrease for droplet radii exceeding 200 μm, which could also indicate the presence of the giant droplets. The absolute values of SGFs are within the experimental uncertainty of the data of Ortiz-Suslow et al. (2016), estimated by the authors as one order of magnitude (see Fig. 10a in Ortiz-Suslow et al., 2016). Note that the difference between the data of Veron et al. (2012) and Ortiz-Suslow et al. (2016) for similar values of u_* is about one order of magnitude, which can be explained by the difference in the conditions of the experiments and the transformation used to infer the SGF from measurements of droplet concentration at different levels (see Ortiz-Suslow et al., 2016). Fig. 13 shows that the main difference of the bag breakup SGF from the data of Veron et al. (2012) and Ortiz-Suslow et al. (2016) is an overestimation of numbers of droplets with radii above 250–300 μm and an underestimation of the number of droplets with radii below 200–250 μm. This may be due to several factors. First of all, strictly speaking, in Fig. 13 we are comparing different features. Veron et al. (2012) and Ortiz-Suslow et al. (2016) did not directly measure the number of droplets ejected from the water surface as assumed by the bag breakup SGF, but, rather, they estimated the number of drops injected from a certain level in terms of a certain model, namely 2.5 H_S in Ortiz-Suslow et al. (2016) and H_S in Veron et al. (2012), where H_S is the significant wave height. At these levels, the concentration of the largest droplets may be significantly lower versus ejection from the surface. This hypothesis is indirectly confirmed by the lower SGF in Ortiz-Suslow et al. (2016) compared to Veron et al. (2012). Underestimation of the number of droplets with radii less than 200–250 μm by the bag breakup SGF can be explained by a contribution from alternative mechanisms of spray production (e.g., bursting of large underwater bubbles described in Section 3.2), which can be more effective in producing smaller droplets. Notice, that the values of SGFs, retrieved from the data of Fairall et al. (2009) significantly exceed those in Ortiz-Suslow et al. (2016) and Veron et al. (2012). Similarly, the bag breakup SGF predicts lower values in comparison with the data of Fairall et al. (2009). Possibly these differences originate from the peculiarities of the mixed regime of surface waves in the experiments by Fairall et al. (2009) combined paddle-generated waves with wind waves. Alternatively, in the present experiments and in the experiments by Ortiz-Suslow et al. (2016) and Veron et al. (2012), pure wind wave regime was used.

We have also verified the bag breakup SGF against data obtained in the field. Among numerous SGFs for spume droplets (see references in Veron (2015) and Andreas (2002)) we selected those suggested by Andreas (1998), Fairall et al. (1994) and Zhao et al. (2006), which are close in magnitude and fit the criteria of reliability suggested by Andreas (2002). The bag breakup SGF was calculated using Eq. (24) with the specific number of bag breakup events defined by Eqs. (7) and (9). Figs. 14a–b show quite good correspondence between our “theoretical+lab-experiment SGF” and the “empirical SGFs” of Andreas (1998), Fairall et al.

(1994), and Zhao et al. (2006) in the radius interval 30μ < r < 300μm. It is by no means surprising that giant rim droplets with r > 300mm are missed in SGFs by Andreas (1998), Fairall et al. (1994), and Zhao et al. (2006), where SGFs were derived through extrapolation of data obtained at winds below 20 m/s (cf. Andreas, 1992), when the bag breakup mechanism was not activated.

7. Summary

This paper focuses on the mechanisms of production of spume droplets, i.e., sea spray torn off wave crests by wind. The study is based on laboratory experiments in a high-speed wind-wave flume, where measurements were performed for airflow with a friction velocity in the range 0.8–1.5 m/s. According to data by Powell et al. (2003) and Richter et al. (2016), this corresponds to the typical range of turbulent shear stresses observed in the turbulent boundary layer under severe tropical storm and hurricane conditions. High-speed video capture enabled us to investigate how droplets are torn from the crests of surface waves. Since the typical timescale of this process is a few milliseconds, frame rates from 4,500 fps to 10,000 fps were used. Capturing video from two directions (side and top view) enabled us to study the process of spume droplet generation in detail. The video revealed that the generation of spume droplets near the wave crest is caused by several local phenomena. It is possible to classify the observed phenomena into three types. One is the development of liquid ligaments, mainly on the crests of breaking waves, which stretch and then break into droplets, as previously observed by Koga (1981). A second is the production of spume droplets through the bursting of submerged bubbles, as was investigated in detail by Lhuissier and Villermaux (2012). The third effective mechanism of spume droplet generation was bag breakup, first observed by Veron et al. (2012). During a bag breakup event, an increase in the small-scale elevation of the water surface results in the formation of a kind of small sail, which is then inflated into a canopy bordered by a thicker rim and finally ruptures to produce spray.

Statistical analysis of the videos showed that bag breakup is the dominant mechanism of spume droplet generation at high winds, when u_* exceeds approximately 1.0 m/s. This mechanism was therefore studied in more detail. The dependency of the specific number of bag breakup events, $\langle N \rangle$ (per unit area per unit time), on wind friction velocity, u_*, in the turbulent boundary layer was derived from the processing of top-view high-speed video frames. These statistics were interpreted using a phenomenological approach based on the methods of statistical physics, specifically the Gibbs canonical ensemble, and the function for $\langle N \rangle$ in terms of u_* was then derived. Expressing $\langle N \rangle$ in terms of the windsea Reynolds number, $\mathrm{Re}_B = u_*^2 / \omega_p \nu$, yields the dependence on wind fetch required for extrapolation to field conditions. The statistical distributions of the sizes, speeds, and lifetimes of the observed bags at different airflow velocities were also investigated, and it was found that all the probability density functions could be well-approximated by the gamma distribution with different parameters.

The statistics obtained for the bag breakup events were used to construct an SGF for the bag breakup mechanism of spray production. First, we took into account that the droplets from a bag are generated via two mechanisms: rupture of the canopy of the inflated bag (the canopy droplets) and fragmentation of the rim that remains after fragmentation of the canopy (rim droplets). To obtain the size distribution of the canopy droplets, we used the results of a detailed study by Lhuissier and Villermaux (2012) on spray generation through the bursting of submerged bubbles, which is very similar to rupture of the canopy of the bag, since both these phenomena are governed by surface tension. To derive the size distribution of the rim droplets, we used the similarity of the bags observed near the crests of breaking surface waves and the development of liquid droplets in gaseous flows in the bag breakup regime. We used the geometrical parameters of bags that have been thoroughly investigated by Chou and Faeth (1998) and the statistics of droplets produced by fragmentation of liquid ligaments suggested in Marmottant and Villermaux (2004). The resultant bag breakup SGF was the sum of the generation of both functions for the canopy and rim droplets. The maxima of these functions slightly decrease with wind friction velocity and are significantly different: for u_*=1–2 m/s, the maximum of the canopy part of the SGF as the volume flux corresponds to a drop radius of approximately 100 μm, while rim fragmentation producing giant droplets has a maximum corresponding to approximately 1000 μm.

The bag breakup SGF derived from our laboratory data was compared with spume droplet SGFs designed for application under both field and laboratory conditions. We compared with the SGFs of Iida et al. (1992), Veron et al. (2012), and Ortiz-Suslov et al. (2016), which were derived from specially designed laboratory experiments. This comparison showed a reasonable agreement of the bag breakup SGF with the data of Veron et al. (2012) and Ortiz-Suslov et al. (2016), although the bag breakup SDF predicts a larger average droplet size. We propose that this may be explained by a lower number of the largest droplets at the measuring points used in the experiments of Veron et al. (2012) and Ortiz-Suslov et al. (2016). The SGF suggested by Iida et al. (1992) shows a very slow decrease for droplet radii exceeding 200 μm, which may also indicate the presence of giant droplets.

We also compared the bag breakup SGF with SFGs developed for field conditions. We employed the bag breakup SGF rescaled to field conditions using a parameterization of the number of bag breakup phenomena by the windsea Reynolds number, as suggested by Toba and Koga (1986). In our estimates, we assumed that the inverse wave age parameter under field conditions, $\Omega = U_{10}/c_p$, was equal to 2.5–3.5 in accordance with the field data of

Wright et al. (2001) and used a surface drag coefficient taken from Holthuijsen et al. (2012). The bag breakup SGF was in reasonable agreement in magnitude with SFGs by Andreas (1992, 1998) and Fairall et al. (1994). We suggested two versions of the model of the fetch dependence of the specific numbers of the bag-breakup events and related SGF, Eq. (7) and Eq.(9). Now the data are not sufficient to give advantage to one of these expressions, however Eq.(7) looks promising, because it predicts realistic essential spray production at wind speeds 10-15 m/s.

The agreement of the bag breakup SGF with both lab and field data confirms our basic hypothesis regarding the dominant role of bag breakup in hurricanes. This result has numerous prospective applications and forms a new basis for modeling the sea-spray and air–sea fluxes. For example, the effect of bag breakup on water-surface resistance can explain the non-monotonous dependence of the surface drag coefficient on wind speed in hurricane winds. Besides, the boosting of exchange processes by giant droplets could be responsible for the significant increase in the air–sea enthalpy flux at high winds that is needed to explain the fast development of intensive hurricanes. These questions are the subject of part II of this study.

Acknowledgements. This work has been supported by the Russian Science Foundation (project 14-17-00667), the Seventh Framework Programme (project PIRSES-GA-2013-612610) and the Russian Foundation for Basic Research (projects 14-17-00667, 16-05-00839, 18-55-50005, 18-05-60299). Sergej Zilitinkevich additionally acknowledges support from the Academy of Finland project ABBA 280700 and ClimEco 314 798/799, Alexander Kandaurov acknowledges support by the President grant for young scientists MC-2041.2017.5. The basic salary of the authors from IAP is financed by the government contract 0035-2014-0032. The experiments were performed at the Unique Scientific Facility "Complex of Large-Scale Geophysical Facilities" (http://www.ckp-rf.ru/usu/77738/).

Appendix A. Statistics of bag breakup events: the Gibbs canonical ensemble approach

This is a summary of the material in the Supplement to Troitskaya et al. (2017).

Originally, the concept of the Gibbs canonical ensemble was developed for a thermodynamic system in weak thermal contact with a heat bath, i.e., an environment that remains at an unchanged temperature due to the negligible feedback of the thermodynamic system to the heat bath. The statistics of the system are determined using the Gibbs or canonical distribution, and the probability that the energy of the system is in the range [E, $E + dE$] is

$$dW = A\exp\left(-E/\vartheta\right)dE\ .$$

The factor $A=1/\vartheta$, according to the normalization condition.

However, the Gibbs method can be applied universally (see Rumer and Ryvkin, 1980) and here it is applied to describing the statistics of bags. We consider the canonical ensemble, which consists of all energy states of the air–ocean interface including those where it can potentially be transformed into bags and then atomized into spray. The analog of the heat bath is the marine atmospheric boundary layer (MABL), which prescribes the state of the interface. Note that the comparatively weak feedback of the state of the air–sea interface to the state of the MABL (an analog of the weakness of the thermal contact of the thermodynamic system to the heat bath) is provided by the small (4–5%, according to Golitsyn (2001)) fraction of wind energy spent to generate surface waves and accompanying phenomena in comparison with turbulent dissipation in the MABL.

The heat bath parameter, ϑ, can be derived from the Boussinesq (1877) analogy between the velocity fluctuations in a turbulent flow and the thermal motions of molecules in a gas. For molecular motion, according to Gibbs (1902), ϑ is proportional to the temperature of the heat bath, i.e., to the average kinetic energy of the molecules. In the problem being considered here, the analog to the temperature of the gas is the kinetic energy density of turbulent fluctuations in the MABL, where the latter is scaled by the wind friction velocity, i.e., $\vartheta \sim u_*^2$.

When the energy of the system under consideration, E, exceeds the threshold, E_0, of activation of the bag breakup regime, the number of bags arising per unit time per unit area of the water surface is a function of the energy state of the air-ocean interface $N(E)$, and the average specific number of bags $\langle N \rangle$ is equal to the integral of $N(E)dW$ over all states with energy exceeding the activation threshold, E_0. In the vicinity of the threshold, $N(E) = N'(E_0)(E - E_0)$ and integrating for $N(E)dW$ yields $\langle N \rangle = N'(E_0)\vartheta e^{-\frac{E_0}{\vartheta}}$. Since $\vartheta \sim u_*^2$,

$$\langle N \rangle (u_*) = Q_0 u_*^2 \exp\left(-\frac{U_0^2}{u_*^2}\right),$$

where Q_0 and U_0 are empirical constants to be derived by fitting of the data.

Appendix B. Derivation of the SGF for the canopy droplets

The total number of droplets with radii in the range [r, $r+\Delta r$] produced by rupture of the canopy of a bag per unit area per unit time is the convolution of the size spectra of bags (Eq. (16)) with the size spectra of droplets generated due to the rupture of the canopy of the inflated bag (Eq. (17)):

$$\frac{dF_c(r,u_*)}{dr} = \frac{\langle N \rangle (u_*)}{\langle R_2 \rangle (u_*)} \times \int_0^\infty \frac{n^n}{\Gamma(n)} \left(\frac{R}{\langle R_2 \rangle (u_*)}\right)^{n-1} e^{-\frac{nR}{\langle R_2 \rangle (u_*)}} N_{\substack{film \\ drops}}(R) \frac{m^m}{\Gamma(m)} \left(\frac{r}{\langle r \rangle (R)}\right)^{m-1} e^{-\frac{mr}{\langle r \rangle (R)}} \frac{dR}{\langle r \rangle (R)} \qquad \text{(B1)}$$

Here, the dependence $\langle R_2\rangle(u_*)$ is given by Eq. (12), $\langle r\rangle(R)$ by Eq. (21), n=7.53, m=11. The limits of integration are chosen equal to 0 and ∞ because the Gamma distribution is a well-localized function that decreases exponentially at infinity.

Substituting expressions for $\langle r\rangle(R)$ and $N_{\substack{film\\drops}}(R)$ from Eqs. (21) and (22) to Eq. (B1) and replacing the variables in the integrand, $R = \langle R_2\rangle(u_*)x$, gives:

$$\begin{aligned}\frac{dF_c(r,u_*)}{dr} &= \langle N\rangle(u_*)\frac{n^n m^m}{\Gamma(n)\Gamma(m)}\left(\frac{n}{m}\right)^{m-1}\frac{b}{aL}\left(\frac{\langle R_2\rangle(u_*)}{L}\right)^{\beta-\alpha}\left(\frac{r}{\delta}\right)^{\frac{m+n-\alpha+\beta-1}{\alpha+1}}\times\\ &\times\int_0^\infty x^{n+\beta-\alpha m-1}\exp\left(-n\left(\frac{r}{\delta}\right)^{\frac{1}{\alpha+1}}\left(x+x^{-\alpha}\right)\right)dx\end{aligned}\qquad \text{(B2)}$$

where $\delta = \dfrac{na\left(\langle R_2\rangle(u_*)\right)^\alpha}{mL^{\alpha-1}}$.

Approximate integration of Eq. (B2) using the method of steepest descent (cf., e.g. Nayfeh, 1981) is applicable if $n\eta$ >>1, where $\eta = (r/\delta)^{1/(\alpha+1)}$. In this case, the factor in Eq. (B2),

$$G(\eta) = \eta^{m+n-\alpha+\beta-1}\int_0^\infty x^{n+\beta-\alpha m-1}\exp\left(-n\eta\left(x+x^{-\alpha}\right)\right)dx\,, \qquad \text{(B3)}$$

is transformed to the following simple expression:

$$G(\eta) \approx G_0\eta^{m+n-\alpha+\beta-\frac{3}{2}}\exp\left(-g_1\eta+\frac{g_2}{\eta}\right), \qquad \text{(B4)}$$

with

$$G_0 = \alpha^{\frac{n+\beta-\alpha m-1/2}{\alpha+1}}\sqrt{\frac{2\pi}{n(\alpha+1)}}\,;\; g_1 = n(\alpha+1)\alpha^{-\frac{\alpha}{\alpha+1}}\,;\; g_2 = \frac{(n+\beta-\alpha m)^2}{2n(\alpha+1)}\alpha^{-\frac{1}{\alpha+1}} \qquad \text{(B5)}$$

Selection of the parameters G_0, g_1 and g_2 in Eq. (B4) by best fitting of the exact expression Eq. (B3) for $G(\eta)$, namely G_0=0.46, g_1=15.12, g_2=0.44, provides an accurate approximation of the factor $G(\eta)$ that is applicable to all relevant values of η.

Using Eq. (B4) to express function $G(\eta)$ defined by Eq. (B3) and substituting it into Eq. (B2) gives:

$$\frac{dF_c(r,u_*)}{dr} = \langle N\rangle(u_*)\frac{n^n m^m}{\Gamma(n)\Gamma(m)}\left(\frac{n}{m}\right)^{m-1}\frac{b}{aL}\left(\frac{\langle R_2\rangle(u_*)}{L}\right)^{\beta-\alpha}\left(\frac{r}{\delta}\right)^{\frac{m+n-\alpha+\beta-3/2}{\alpha+1}} \times$$
$$\times G_0 \exp\left(-g_1\left(\frac{r}{\delta}\right)^{\frac{1}{(\alpha+1)}} + g_2\left(\frac{\delta}{r}\right)^{\frac{1}{(\alpha+1)}}\right)$$

where $\delta = \dfrac{na\left(\langle R_2\rangle(u_*)\right)^{\alpha}}{mL^{\alpha-1}}$.

Simple algebra yields the following symmetrical form of the exponent:

$$\frac{dF_c(r,u_*)}{dr} = \langle N\rangle(u_*)\frac{n^n m^m}{\Gamma(n)\Gamma(m)}\left(\frac{n}{m}\right)^{m-1}\frac{b}{aL}\left(\frac{\langle R_2\rangle(u_*)}{L}\right)^{\beta-\alpha}\left(\frac{r}{\theta}\right)^{\frac{m+n-\alpha+\beta-3/2}{\alpha+1}} \times$$
$$\times G_0\left(\frac{g_2}{g_1}\right)^{\frac{m+n-\alpha+\beta-3/2}{2}} \exp\left(-2\sqrt{g_1 g_2}\sinh\left(\frac{1}{\alpha+1}\ln\frac{r}{\theta}\right)\right),$$

where

$$\theta = \frac{na\left(\langle R_2\rangle(u_*)\right)^{\alpha}}{mL^{\alpha-1}}\left(\frac{g_2}{g_1}\right)^{\frac{\alpha+1}{2}}.$$

Substituting numbers for n=7.53, m=11,

$a = 0.094$, $\alpha = 4/3$ $b = 2.24\cdot 10^{-3}\left(\dfrac{\rho_w g L^2}{\sigma}\right)^{1.18}$, $\beta \approx 4/3$, G_0=0.46, g_1=15.12, and g_2=0.44

finally gives:

$$\frac{dF_c(r,u_*)}{dr} = \frac{3.3\cdot 10^{-9}}{L}\langle N\rangle(u_*)\left(\frac{\rho_w g L^2}{\sigma}\right)^{1.18}\left(\frac{r}{\theta}\right)^{7.3} e^{-5.2\sinh\left(\frac{3}{7}\ln\frac{r}{\theta}\right)}, \quad \text{(B6)}$$

$$\theta = \frac{0.001\left(\langle R_2\rangle(u_*)\right)^{4/3}}{L^{1/3}}. \quad \text{(B7)}$$

Appendix C. Derivation of the expression for the SGF for rim droplets

The total number of rim droplets with radii in the range [r,$r+\Delta r$] produced by bags per unit area per unit time is the convolution of the size spectra of bags (Eq. (16)) with the size spectra of droplets generated due to the fragmentation of the rim (Eq. (23)):

$$\frac{dF_{rim}(r,u_*)}{dr}=\frac{\langle N\rangle(u_*)N_{\substack{rim\\drops}}}{\langle R_2\rangle(u_*)}\int_0^\infty\frac{n^n}{\Gamma(n)}\left(\frac{R}{\langle R_2\rangle(u_*)}\right)^{n-1}e^{-\frac{nR}{\langle R_2\rangle(u_*)}}\frac{k^k}{\Gamma(k)}\left(\frac{r}{\gamma R}\right)^{k-1}e^{-\frac{kr}{\gamma R}}\frac{dR}{\gamma R}.$$

Replacing the variables in the integrand, $R=\langle R_2\rangle(u_*)x$, yields:

$$\frac{dF_{rim}(r,u_*)}{dr}=\frac{\langle N\rangle(u_*)N_{\substack{rim\\drops}}}{\gamma\langle R_2\rangle(u_*)}\frac{n^n}{\Gamma(n)}\frac{k^k}{\Gamma(k)}\left(\frac{k}{n}\right)^{\frac{n-k}{2}}\left(\frac{r}{\gamma\langle R_2\rangle(u_*)}\right)^{\frac{n+k}{2}-1}\int_0^\infty x^{n-k-1}e^{-\sqrt{\frac{knr}{\gamma\langle R_2\rangle(u_*)}}\left(x+\frac{1}{x}\right)}dx$$

(C1)

Introducing the new variable, $\varepsilon=\sqrt{r/\Delta}$, where $\Delta=\gamma\langle R_2\rangle(u_*)$, and using the method of steepest descent, similarly to Appendix B, we can transform the factor

$\Phi(\varepsilon)=\varepsilon^{n+k-2}\int_0^\infty x^{n-k-1}e^{-\varepsilon\sqrt{kn}\left(x+\frac{1}{x}\right)}dx$ in (C1) to

$$\Phi_{app}(\varepsilon)=\Phi_0\varepsilon^{n+k-\frac{5}{2}}e^{-\phi_1\varepsilon+\frac{\phi_2}{\varepsilon}}, \qquad \text{(C2)}$$

with

$$\phi_1=2\sqrt{kn},\ \phi_2=\frac{(n-k)^2}{4\sqrt{kn}},\ \Phi_0=\sqrt{\frac{\pi}{\sqrt{kn}}}. \qquad \text{(C3)}$$

Similarly to in Appendix B, we can find ϕ_1, ϕ_2, and Φ_0, which enables an accurate fit for $\Phi(\varepsilon)$ by use of function (C2): ϕ_1=11.07, ϕ_2 = 0.35, and Φ_0=1.02.

Substituting Eq. (C2) into Eq. (C1) gives:

$$\frac{dF_{rim}(r,u_*)}{dr}=\frac{\langle N\rangle(u_*)N_{\substack{rim\\drops}}}{\Delta}\frac{n^n}{\Gamma(n)}\frac{k^k}{\Gamma(k)}\left(\frac{k}{n}\right)^{\frac{n-k}{2}}\left(\frac{r}{\Delta}\right)^{\frac{n+k}{2}-\frac{5}{4}}\Phi_0\exp\left(-\phi_1\left(\frac{r}{\Delta}\right)^{\frac{1}{2}}+\phi_2\left(\frac{\Delta}{r}\right)^{\frac{1}{2}}\right) \qquad \text{(C4)}$$

Simple algebra yields the symmetrical form of the exponent in Eq. (C4):

$$\frac{dF_{rim}(r,u_*)}{dr} = \frac{\langle N\rangle(u_*)\, N_{\substack{rim\\drops}}}{\Theta} \frac{n^n}{\Gamma(n)} \frac{k^k}{\Gamma(k)} \left(\frac{k}{n}\right)^{\frac{n-k}{2}} \left(\frac{r}{\Theta}\right)^{\frac{n+k}{2}-\frac{5}{4}} \Phi_0 \left(\frac{\phi_2}{\phi_1}\right)^{\frac{n+k}{2}-\frac{1}{4}} e^{-2\sqrt{\phi_1\phi_2}\,\sinh\left(\frac{1}{2}\ln\frac{r}{\Theta}\right)},$$

where $\Theta = \gamma\langle R_2\rangle(u_*)\phi_2/\phi_1$.

Substituting numbers for n=7.53, k=4, γ=0.068, ϕ_1=11.07, ϕ_2 = 0.35, and Φ_0=1.02 finally yields:

$$\frac{dF_{rim}(r,u_*)}{dr} = \langle N\rangle(u_*) \frac{1.5\cdot 10^{-4} N_{\substack{rim\\drops}}}{\Theta} \left(\frac{r}{\Theta}\right)^{4.5} e^{-3.94\sinh\left(\frac{1}{2}\ln\frac{d}{\Theta}\right)}, \qquad \text{(C5)}$$

$$\Theta = 0.0021\langle R_2\rangle(u_*). \qquad \text{(C6)}$$

References

Andreas, E. L., 1992: Sea spray and the turbulent air–sea heat fluxes. *J. Geophys. Res.*, **97,** 11429–11441, https://doi.org/10.1029/92JC00876.

Andreas, E. L., 1998: A New Sea Spray Generation Function for Wind Speeds up to 32 m s^{-1}. *J. Phys. Oceanogr.*, **28,** 2175–2184, https://doi.org/10.1175/1520-0485(1998)028<2175:ANSSGF>2.0.CO;2.

Andreas, E. L., 2002: A review of spray generation function for the open ocean. *Atmosphere-Ocean Interactions Volume 1*, Perrie, W., Ed., WIT Press, 1–46.

Andreas, E. L., 2011: Fallacies of the Enthalpy Transfer Coefficient over the Ocean in High Winds. *J. Atmos. Sci.*, **68,** 1435–1445, https://doi.org/10.1175/2011JAS3714.1.

Andreas, E. L., and K. A. Emanuel, 2001: Effects of Sea Spray on Tropical Cyclone Intensity. *J. Atmos. Sci*., **58,** 3741–3751, https://doi.org/10.1175/1520-0469(2001)058<3741:EOSSOT>2.0.CO;2.

Bao, J.-W., C. W., Fairall, S. A. Michelson, and L. Bianco: 2011: Parameterizations of sea-spray impact on the air–sea momentum and heat fluxes. *Mon. Weather Rev.*, **139,** 3781–3797, https://doi.org/10.1175/MWR-D-11-00007.1.

Bianco, L., J.-W. Bao, C. W. Fairall, and S. A. Michelson, 2011: Impact of sea spray on the surface boundary. *Bound.-Layer Meteor*., **140**, 361–381, https://doi.org/10.1007/s10546-011-9617-1.

Blanchard, D. C., 1963: The electrification of the atmosphere by particles from bubbles in the sea. *Prog. Oceanogr*., **1**, 71–202, https://doi.org/10.1016/0079-6611(63)90004-1.

Boussinesq, J. V., 1877: Essai sur la theorie des eaux courantes. *Mémoires présentés par Divers savants à l'Acad. des Sci. Inst. Nat. Fr.*, **XXIII**, 1–680.

Chou W. H., and G. M. Faeth, 1998: Temporal properties of secondary drop breakup in the bag breakup regime. *Int. J. Multiphase Flow*, **24**, 889–91, https://doi.org/10.1016/S0301-9322(98)00015-9.

Fairall, C. W., J. D. Kepert, and G. J. Holland, 1994: The effect of sea spray on surface energy transports over the ocean, *Global Atmos. Ocean Syst.*, **2**, 121–142.

Fairall, C. W., M. L. Banner, W. L. Peirson, W. Asher, and R. P. Morison, 2009: Investigation of the physical scaling of sea spray spume droplet production, *J. Geophys. Res. Ocean.*, **114**, C10001, doi.org/10.1029/2012JC007983.

Foreman, R. J., and S. Emeis, 2010: Revisiting the Definition of the Drag Coefficient in the Marine Atmospheric Boundary Layer. *J. Phys. Oceanogr.*, **40,** 2325–2332, https://doi.org/10.1175/2010JPO4420.1.

Gelfand, B. E., 1996: Droplet breakup phenomena in flows with velocity lag. *Prog. Energ. Combust. Sci.*, **22**, 201–265, https://doi.org/10.1016/S0360-1285(96)00005-6.

Gibbs, J. W., 1902: *Elementary Principles in Statistical Mechanics*. Charles Scribner's Sons, 239 pp.

Golitsyn, G. S., 2010: The energy cycle of wind waves on the sea surface *Izv. Atmos. Ocean. Phys*., **46**, 6-13, https://doi.org/10.1134/S0001433810010020.

Hinze, J.O., 1959: *Turbulence.* 2nd Edition, McGraw Hill, 586 pp.

Holthuijsen, L. H., M. D. Powell, and J. D. Pietrzak, 2012: Wind and waves in extreme hurricanes. *J. Geophys. Res. Ocean.*, **117**, C09003, https://doi.org/10.1029/2012JC007983.

Iida, N., Y. Toba, and M. Chaen, 1992: A new expression for the production rate of sea water droplets on the sea surface. *J. Oceanogr.*, **48**, 439–460, https://doi.org/10.1007/BF02234020.

Koga, M. 1981: Direct production of droplets from breaking wind-waves—its observation by a multi-colored overlapping exposure photographing technique. *Tellus*, **33**, 552–563, https://doi.org/10.3402/tellusa.v33i6.10776.

Lhuissier, H., and E. Villermaux, 2009: Bursting bubbles. *Phys. Fluids*, **21**, 091111, https://doi.org/10.1063/1.3200933.

Lhuissier, H., and E. Villermaux, 2012: Bursting bubble aerosols. *J. Fluid Mech.*, **696,** 5–44, https://doi.org/10.1017/jfm.2011.418.

Marmottant, P., and E. Villermaux, 2004: On spray formation. *J. Fluid Mech.*, **498**, 73–111, https://doi.org/10.1017/S0022112003006529.

Mueller, J. A., and F. Veron, 2009: A Sea State–Dependent Spume Generation Function. *J. Phys. Oceanogr.*, **39**, 2363–2372, https://doi.org/10.1175/2009JPO4113.1.

Nayfeh, A. H., 1981: *Introduction to perturbation techniques.* Wiley & Sons, 666 pp.

Ortiz-Suslow, D. G., B. K. Haus, S. Mehta, and N. J. Laxague, 2016: Sea Spray Generation in Very High Winds. *J. Atmos. Sci.* **73**, 3975–3995, https://doi.org/10.1175/JAS-D-15-0249.1.

Petersen, P., 1927: Zur Bestimmung der Windstärke auf See. Für Segler, Dampfer und Luftfahrzeige. *Annalen der Hydrographie und Maritimen Meteorologie*, **55**, 69-72.

Powell, M. D., P. J. Vickery, and T. A. Reinhold, 2003: Reduced drag coefficient for high wind speeds in tropical cyclones. *Nature*, **422**, 279–283, https://doi.org/10.1038/nature01481.

Richter, D. H., R. Bohac, and D. P. Stern, 2016: An assessment of the flux profile method for determining air–sea momentum and enthalpy fluxes from dropsonde data in tropical cyclones. *J. Atmos. Sci.*, **73**, 2665–2682, https://doi.org/10.1175/JAS-D-15-0331.1.

Rumer Yu. B. and M. S. Ryvkin, 1980*: Thermodynamics, statistical physics, and kinetics* (English translation). Mir, 600 pp.

Soloviev, A. V, R. Lukas, M. Donelan, B. K. Haus, and I. Ginis, 2014: The air-sea interface and surface stress under tropical cyclones. *Sci. Rep.* **4,** 5306, https://doi.org/10.1038/srep05306.

Spiel, D. E., 1994a: The number and size of jet drops produced by air bubbles bursting on a fresh water surface. *J. Geophys. Res*., **99**, 10289–96, https://doi.org/10.1029/94JC00382.

Spiel, D. E., 1994b: The sizes of jet drops produced by air bubbles bursting on sea- and fresh-water surfaces. *Tellus B*, **46**, 4, 325–338, https://doi.org/10.3402/tellusb.v46i4.15808.

Spiel, D. E., 1995: On the births of jet drops from bubbles bursting on water surfaces. *J. Geophys. Res.*, **100**, 4995–5006, https://doi.org/10.1029/94JC03055.

Spiel, D. E., 1997: More on the births of jet drops from bubbles bursting on seawater surfaces. *J. Geophys. Res*., **102**, 5815–5821, https://doi.org/10.1029/96JC03582.

Spiel DE., 1998: On the births of film drops from bubbles bursting on seawater surfaces. *J. Geophys. Res.*, **103**, 24907–24918, https://doi.org/10.1029/98JC02233.

Takagaki, N., S. Komori, N. Suzuki, K. Iwano, T. Kuramoto, S. Shimada, R. Kurose, and K. Takahashi, 2012: Strong correlation between the drag coefficient and the shape of the wind sea spectrum over a broad range of wind speeds. *Geophys. Res. Lett.*, **39**, https://doi.org/10.1029/2012GL053988.

Takagaki, N., S. Komori, N. Suzuki, K. Iwano, and R. Kurose, 2016: Mechanism of drag coefficient saturation at strong wind speeds. *Geophys. Res. Lett.*, **43**, 9829–9835, https://doi.org/10.1002/2016GL070666.

Takagaki, N., S. Komori, M. Ishida, K. Iwano, R. Kurose, and N. Suzuki, 2017: Loop-Type Wave-Generation Method for Generating Wind Waves under Long-Fetch Conditions. *J. Atmos. Oceanic Technol*., **34**, 2129–2139, https://doi.org/10.1175/JTECH-D-17-0043.1.

Toba, Y. and M. Koga, 1986: A parameter describing overall conditions of wave breaking, whitecapping, sea-spray production and wind stress. *Oceanic Whitecaps,* E.C. Monahan and G. MacNiocaill, Eds., D. Reidel Publishing Company, 37–47.

Toba, Y., S. Komori, Y. Suzuki, and D. Zhao, 2006: Similarity and dissimilarity in air-sea momentum and CO_2 transfers: The nondimensional transfer coefficients in light of windsea Reynolds number, *Atmosphere-Ocean Interaction*s, 2, W. Perrie, Ed., WIT Press, 53–82.

Troitskaya, Y. I., D. A. Sergeev, A. A. Kandaurov, G. A Baidakov, M. A. Vdovin, and V. I. Kazakov, 2012: Laboratory and theoretical modeling of air-sea momentum transfer under severe wind conditions. *J. Geophys. Res. Ocean.*, **117,** C00J21, https://doi.org/10.1029/2011JC007778.

Troitskaya, Y. I., A. Kandaurov, O. Ermakova, D. Kozlov, D. Sergeev, and S. Zilitinkevich, 2017: Bag-breakup fragmentation as the dominant mechanism of sea-spray production in high winds. *Sci. Rep.*, **7,** 1614, https://doi.org/10.1038/s41598-017-01673-9.

Veron F., 2015: Ocean Spray. *Annu. Rev. Fluid Mech*., **47**, 507–538, https://doi.org/10.1146/annurev-fluid-010814-014651.

Veron, F., C. Hopkins, E. L. Harrison, and J. A. Mueller, 2012: Sea spray spume droplet production in high wind speeds. *Geophys. Res. Lett.*, **39,** L16602, https://doi.org/10.1029/2012GL052603.

Wright, C. W., and Coauthors, 2001: Hurricane Directional Wave Spectrum Spatial Variation in the Open Ocean. *J. Phys. Oceanogr.*, **31**, 2472–2488, https://doi.org/10.1175/1520-0485(2001)031<2472:HDWSSV>2.0.CO;2.

Wu, J., 1981: Evidence of sea spray produced by bursting bubbles. *Science*, **212**, 324.

Zhao, D., Y. Toba, K. Sugioka, and S. Komori, 2006: New sea spray generation function for spume droplets. *J. Geophys. Res. Ocean.*, **111**, C02007.

Tables

Table 1. Parameters of the experiments.

Frequency of the fan (Hz)	Friction velocity (m/s)	Number of records	Total number of frames
30	0.753	1	33452
31	0.814	1	33452
32	0.874	2	66248
33	0.931	5	164636
34	0.987	15	490996
35	1.04	11	360452
36	1.09	11	360452
37	1.15	7	229588
38	1.20	5	164316
39	1.24	3	98884
40	1.29	3	98884
42	1.38	1	33452
45	1.51	2	66248
	Total:	67	2234512

Figure caption list

Fig. 1. Wind and wave parameters in the flume. (a) The roughness height due to the friction velocity in the flume, with the best fit from Eq. (1). (b) The dependency of the peak frequency in the wind wave spectra on wind friction velocity, with the best fit from Eq. (2).

Fig. 2. Schematic diagram of experimental setup.

Fig. 3. Generation of droplets through the development and breakage of liquid ligaments. (a) Stretching of the ligament, t=0 ms. (b) Formation of the droplet, t=3.9 ms. (c) Separation of the first droplet and formation of the second, t=9.3 ms. (d) Formation of the third and fourth droplets, t=17.3 ms, wind speed U_{10}≈25 m/s, image dimensions 67.48×101.13 mm. (e) Spray generation at the crest of the breaking waves (photo taken by Troitskaya at the Gorky reservoir, Volga river, Oct. 1, 2011). Wind speed U_{10}≈9 m/s. Insets 1 and 2 show the magnified details of the wave crest.

Fig. 4. The burst of a large bubble in strong wind conditions, U_{10}=25 m/s. The top panel: (a) The floating bubble, t=0 ms. (b) Formation of a hole in the liquid film, t=3.2 ms. (c) Expansion of the hole, t=5.1 ms. (d) Droplet formation, t=8.4 ms. The bottom panel is the side view of the bubble burst.

Fig. 5. The formation and rupture of a bag. A single bag: (a) side view, (b) top view. A "multi-bag": (c) side view, (d) top view. U_{10}=25 m/s.

Fig. 6. Schematic diagram of the formation and fragmentation of a bag. (a) Formation of the initial disturbance, (b) increase of the initial disturbance, (c) sail-shaped disturbance, (d) formation of the bag, (e) rupture of the bag. The thin dotted lines are the streamlines in the reference frame following the elevation in the water surface.

Fig. 7. Semi-automatic registering of the evolution of a bag: (a) initial frame showing bag nucleation, (b) intermediate frame with annotated markers, edge positions are interpolated, (c) final frame showing the moment of canopy puncture. 1- bag nucleation, 2 - canopy

puncture, 3 - manually defined markers. The friction velocity of the airflow is 1.04 m/s, and the average wind direction is from top to bottom.

Fig. 8. Dependence of the specific numbers (per unit time per unit area) of the spray-generating phenomena (a) on the wind friction velocity and (b) on the windsea Reynolds number. Open circles – bursting of floating bubbles, squares - liquid filaments, closed circles – bag breakup events (Fig. 8a is adopted from Troitskaya et al. (2017)). (c) 10-m wind speed versus wave-age parameter $\Omega = U_{10}/c_p$ at a fixed windsea Reynolds numbers, Re_B, equal to 4000, corresponding to the first appearance of bag breakup (solid curve) and 8000 (dashed curve).

Fig. 9. Approximation of the experimental dependence of specific number of bags on friction velocity (a) using Eq. (5) and (b) on the windsea Reynolds number using Eq.(7). Open symbols are data obtained by processing individual 33,000-frame ~~videos~~ records, and closed symbols are the averaged data; the error bars are defined by the standard deviation. (c) Estimated specific number of bags using field conditions versus U_{10} for the wave-age parameter Ω=2.5 (black curves) and Ω=3.5 (grey curves); solid curves - Eq. (7), dashed curves - Eq. (9).

Fig. 10. (a) The frequency distribution of bag size at the moment of nucleation ($R_1/\langle R_1\rangle$ and at the moment of rupture ($R_2/\langle R_2\rangle$. (b) The frequency distribution of the velocity of the motion of bag edges ($u_1/\langle u_1\rangle$ and centers ($u_2/\langle u_2\rangle$. (c) The frequency distribution of bag lifetime ($\tau/\langle\tau\rangle$. Curves are the Gamma distribution for (a) n = 7.53, (b) n = 13.30, and (c) n = 3.70.

Fig. 11. Dependencies of averaged values on the friction velocity of the air flow: (a) the initial (closed circles) and final size (open diamonds) of bags, (b) the velocity of the edges (closed circles) and centers (open diamonds) of bags, and (c) the lifetime of bags. Lines are the power best fit from Eqs. (11-15). (d) Proportionality in the sizes of bags.

Fig. 12. (a) The bag breakup SGF. (b) The SGFs for the canopy (dash-dot curve) and rim (dashed curve) droplets and their aggregate (gray solid curve) for u_*=1.5 m/s. (c) Bag breakup SGF as the volume flux. For (a) and (c), u_* varies from 1 m/s to 2 m/s with an increment 0.1 m/s.

Fig. 13. Comparison of the bag breakup SGF (solid and dashed lines) with empirical estimations of SGFs under laboratory conditions. Symbols: Iida et al. (1992) - open circles; Ortiz-Suslow et al. (2016) - open squares - u_*=1.75 m/s (U_{10}=36 m/s), closed circles - u_*=1.97 m/s (U_{10}=40.5 m/s), upward-pointing triangles - u_*=2.19 m/s (U_{10}=45 m/s), closed squares - u_*=2.43 m/s (U_{10}=49.5 m/s), downward-pointing triangles - u_*=2.66 m/s (U_{10}=54 m/s); Veron et al. (2012) - crosses - u_*=1.98 m/s (U_{10}=41.2 m/s), X - u_*= 2.33 m/s (U_{10}=47.1 m/s). Fairall et al. (2009) - thin lines with symbols: open diamonds u_*= 1.35 m/s, closed diamonds u_*= 1.44 m/s, closed triangles u_*= 1.64 m/s. For the bag breakup SGF, u_* varies between 1.6 m/s and 2.4 m/s with an increment of 0.2 m/s. Solid lines correspond to u_*=2 m/s (lower) and u_*=2.4 m/s (upper).

Fig. 14. Comparison of the bag breakup SGF with empirical SGFs under field conditions by Andreas (1998) (diamonds), Fairall et al. (1994) (triangles), Zhao et al. (2006) (circles) at U_{10}=30 m/s (a) and U_{10}=35 m/s (b). In the bag breakup SGF, the wave-age parameter Ω=2.5 (black curves) and Ω=3.5 (grey curves); solid curves - Eq. (7), dashed curves - Eq. (9).

Figures

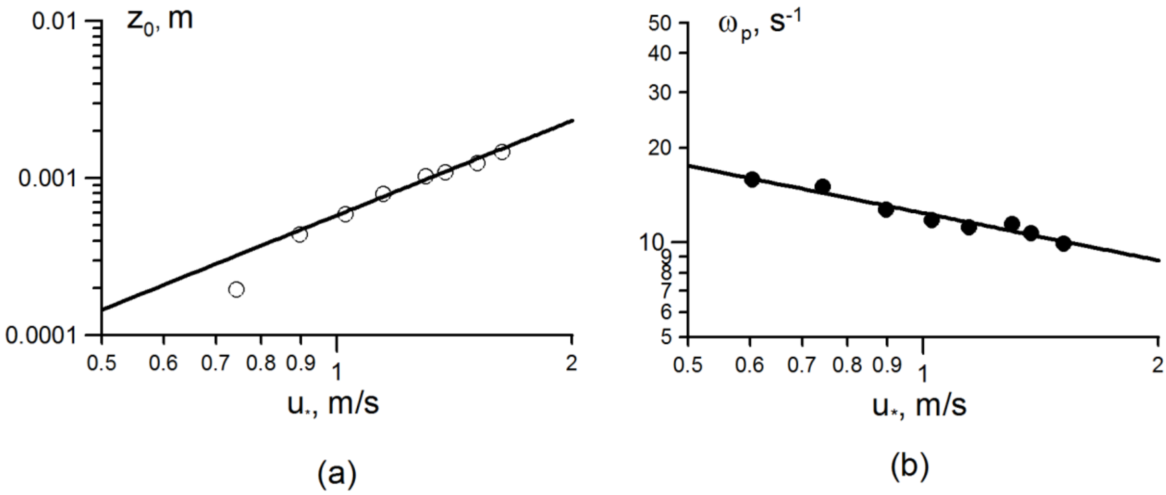

Fig. 1. Wind and wave parameters in the flume. (a) The roughness height due to the friction velocity in the flume, with the best fit from Eq. (1). (b) The dependency of the peak frequency in the wind wave spectra on wind friction velocity, with the best fit from Eq. (2).

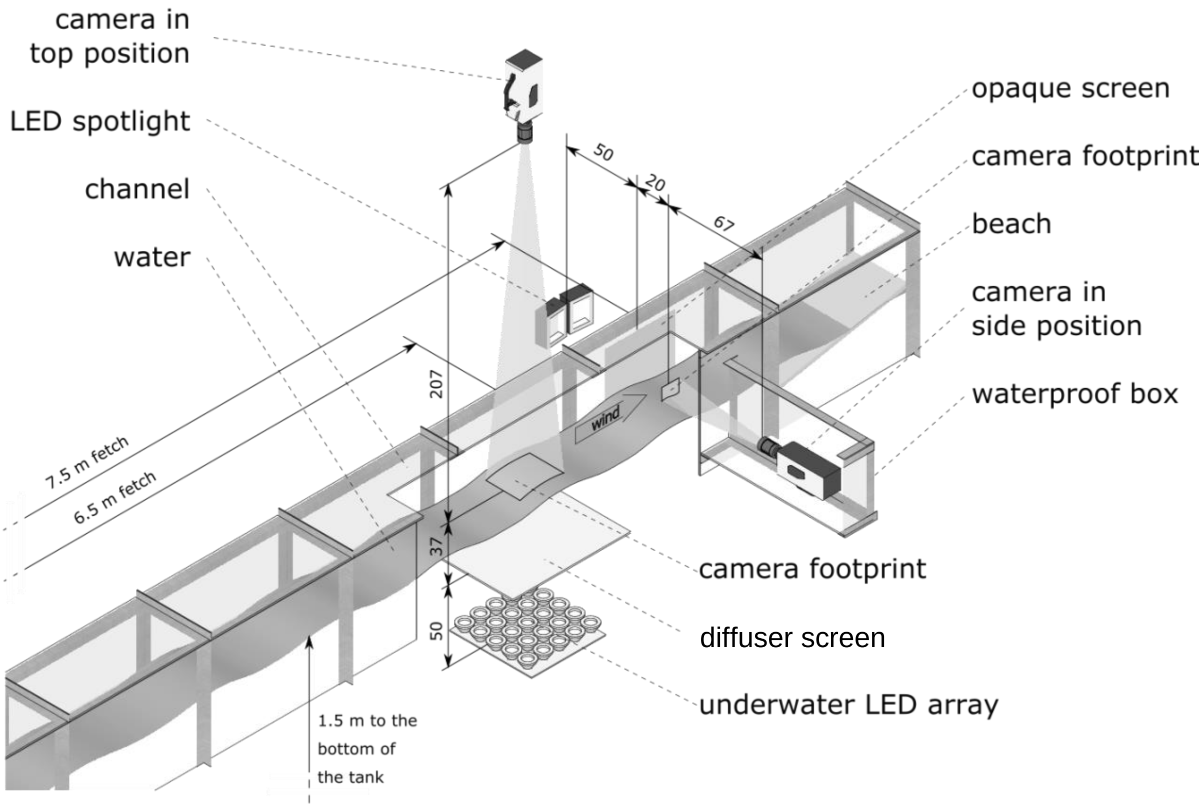

Fig. 2. Schematic diagram of experimental setup.

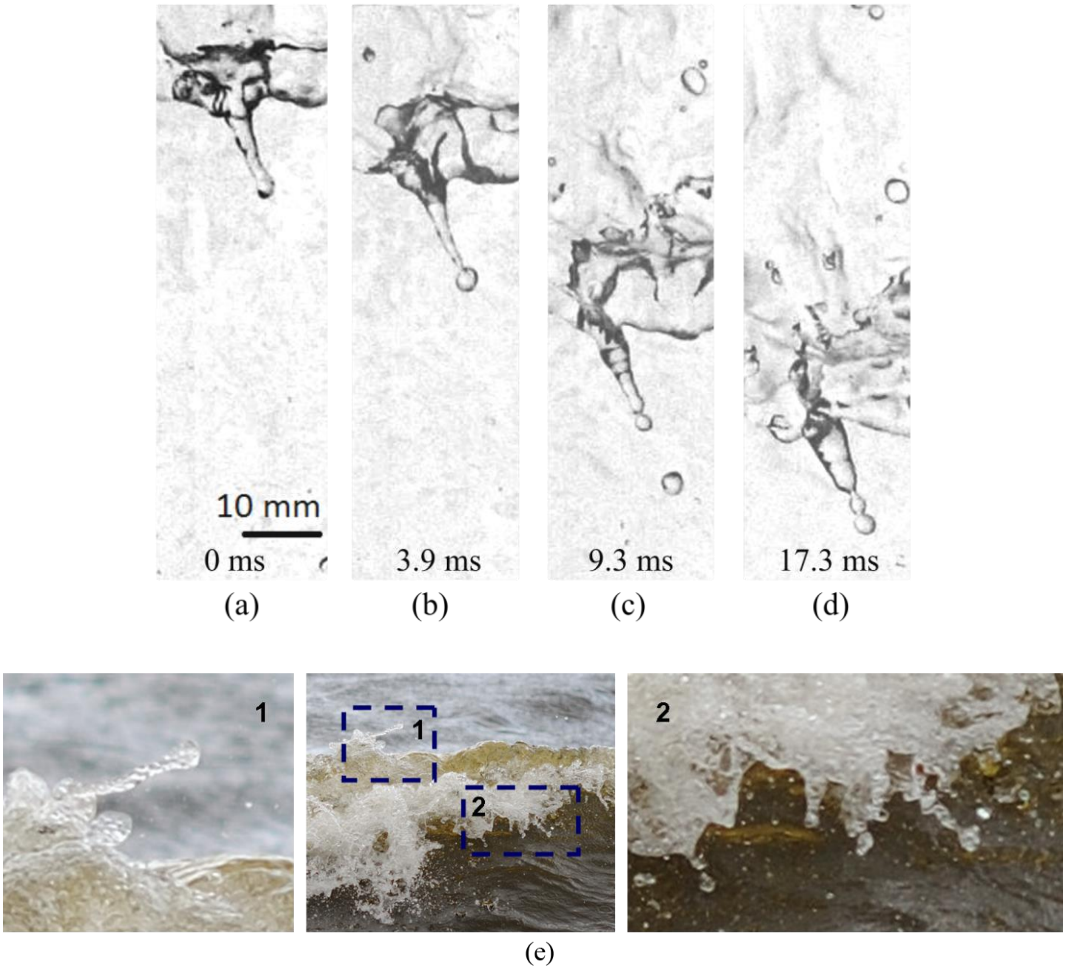

Fig. 3. Generation of droplets through the development and breakage of liquid ligaments. (a) Stretching of the ligament, t=0 ms. (b) Formation of the droplet, t=3.9 ms. (c) Separation of the first droplet and formation of the second, t=9.3 ms. (d) Formation of the third and fourth droplets, t=17.3 ms, wind speed U_{10}≈25 m/s, image dimensions 67.48×101.13 mm. (e) Spray generation at the crest of the breaking waves (photo taken by Troitskaya at the Gorky reservoir, Volga river, Oct. 1, 2011). Wind speed U_{10}≈9 m/s. Insets 1 and 2 show the magnified details of the wave crest.

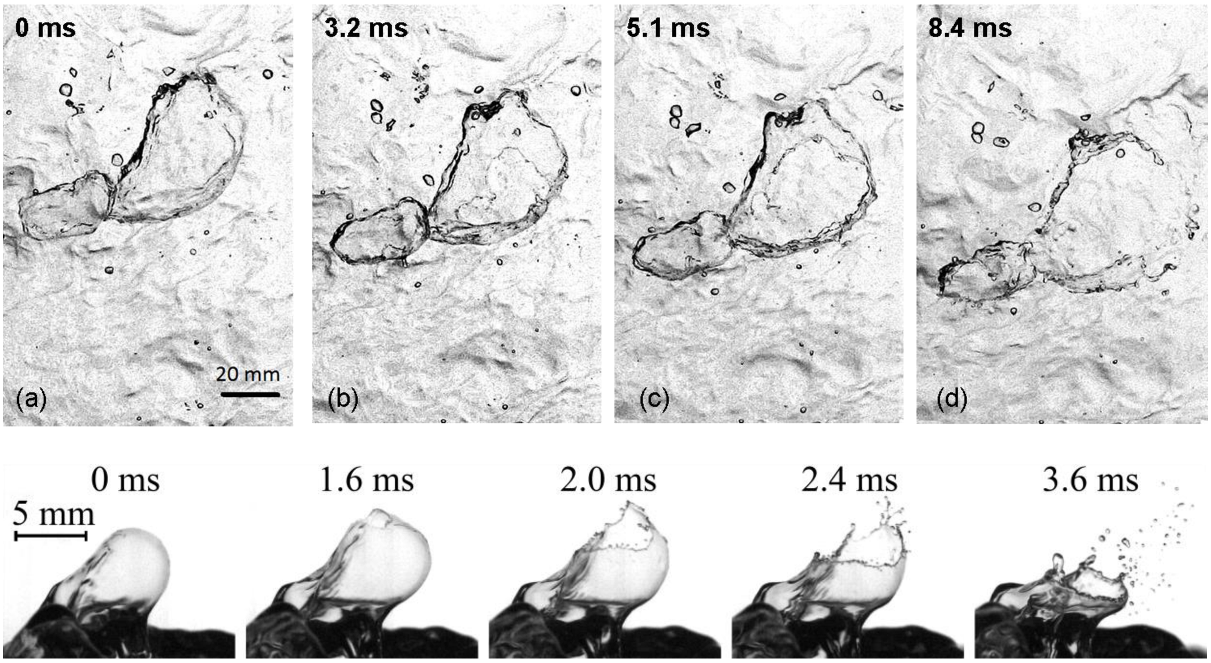

Fig. 4. The burst of a large bubble in strong wind conditions, U_{10}=25 m/s. The top panel: (a) The floating bubble, t=0 ms. (b) Formation of a hole in the liquid film, t=3.2 ms. (c) Expansion of the hole, t=5.1 ms. (d) Droplet formation, t=8.4 ms. The bottom panel is the side view of the bubble burst.

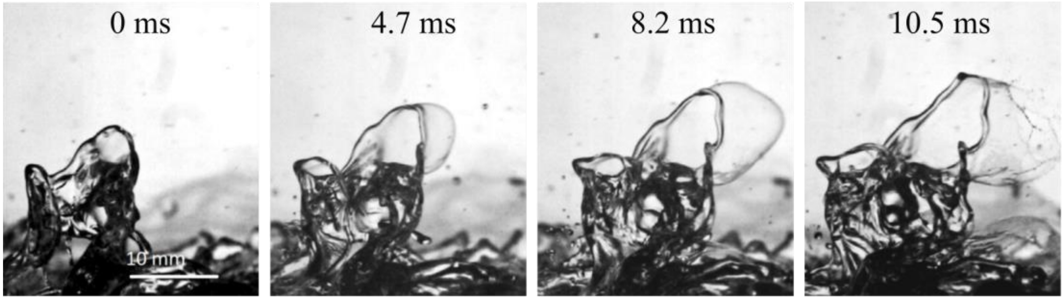

(a)

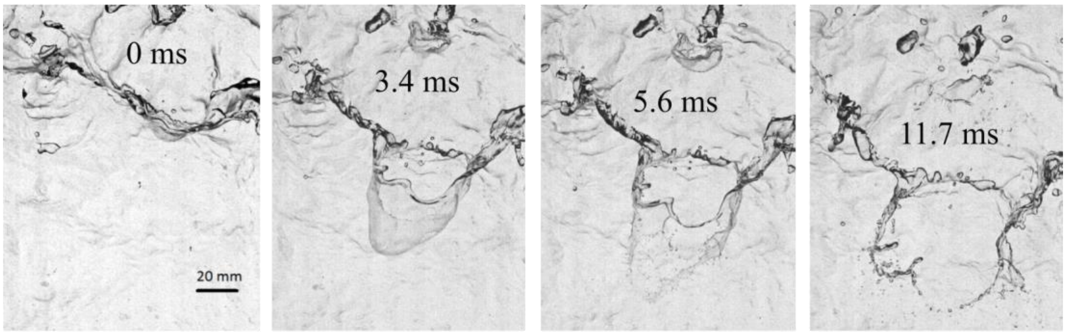

(b)

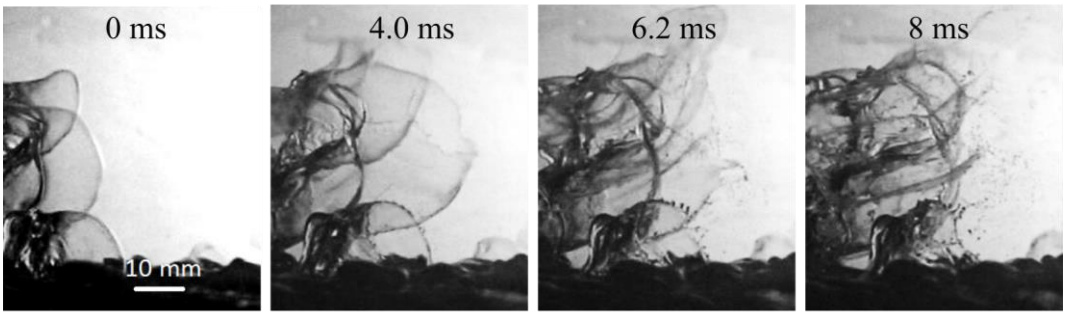

(c)

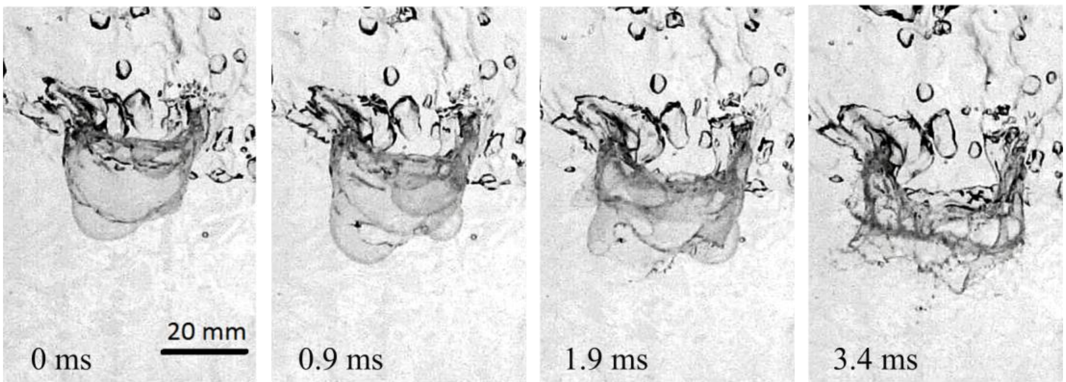

(d)

Fig. 5. The formation and rupture of a bag. A single bag: (a) side view, (b) top view. A "multi-bag": (c) side view, (d) top view. U_{10}=25 m/s.

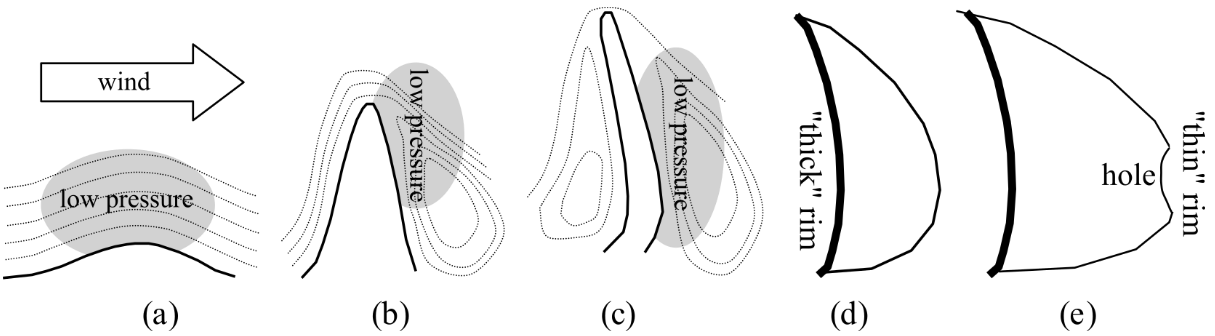

Fig. 6. Schematic diagram of the formation and fragmentation of a bag. (a) Formation of the initial disturbance, (b) increase of the initial disturbance, (c) sail-shaped disturbance, (d) formation of the bag, (e) rupture of the bag. The thin dotted lines are the streamlines in the reference frame following the elevation of the water surface.

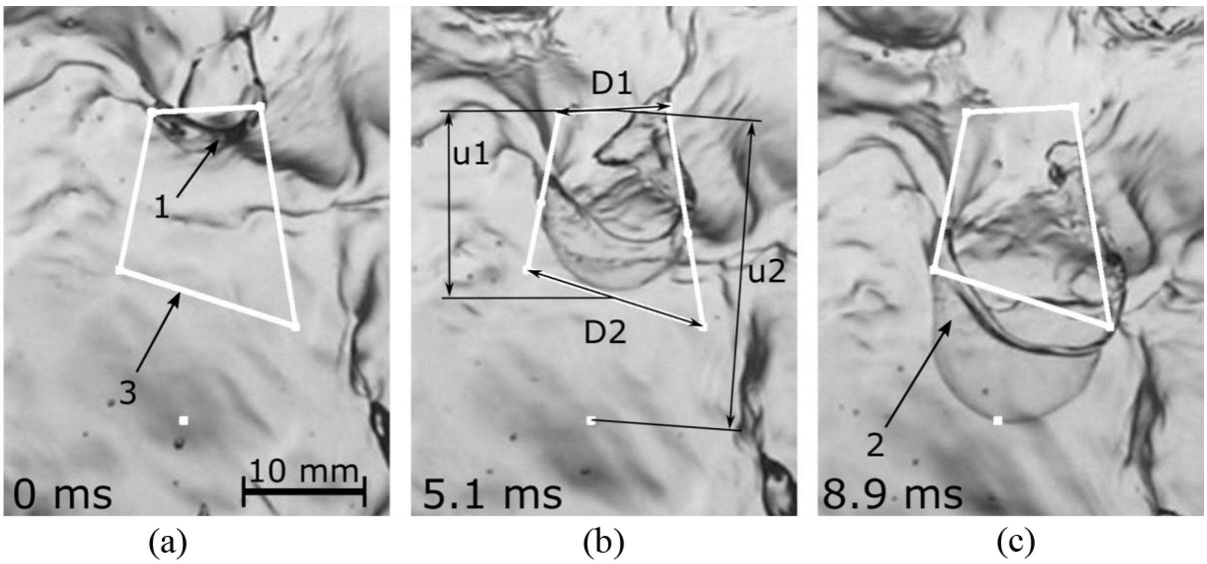

Fig. 7. Semi-automatic registering of the evolution of a bag: (a) initial frame showing bag nucleation, (b) intermediate frame with annotated markers, edge positions are interpolated, (c) final frame showing the moment of canopy puncture. 1- bag nucleation, 2 - canopy puncture, 3 - manually defined markers. The friction velocity of the airflow is 1.04 m/s, and the average wind direction is from top to bottom.

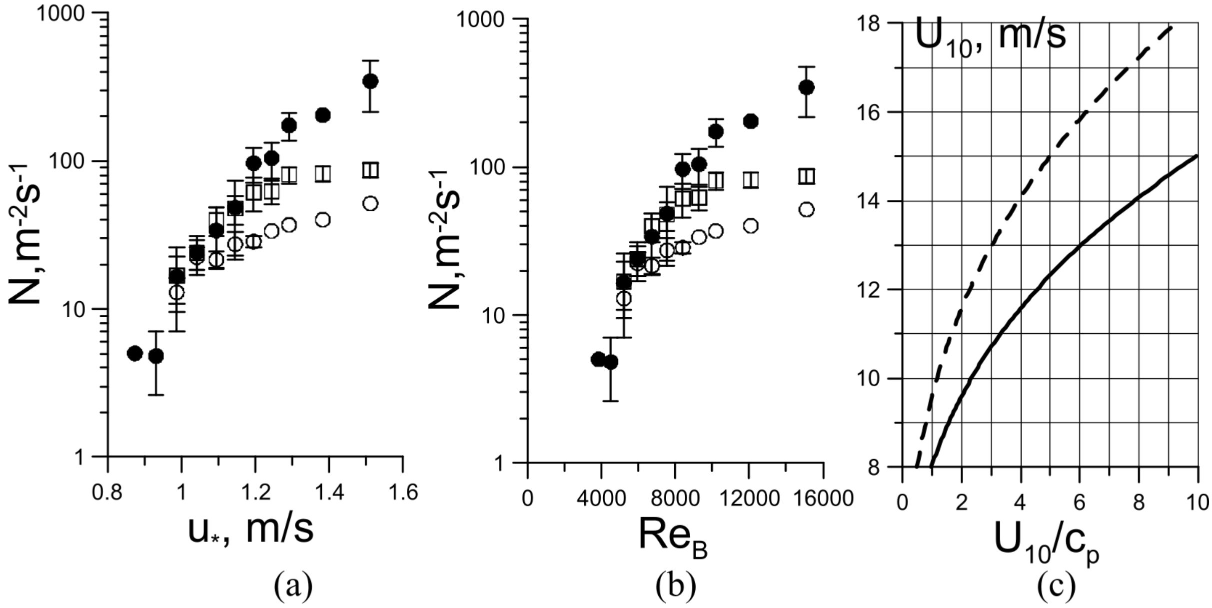

Fig. 8. Dependence of the specific numbers (per unit time per unit area) of the spray-generating phenomena (a) on the wind friction velocity and (b) on the windsea Reynolds number. Open circles – bursting of floating bubbles, squares - liquid filaments, closed circles – bag breakup events (Fig. 8a is adopted from Troitskaya et al. (2017)). (c) 10-m wind speed versus wave-age parameter $\Omega = U_{10}/c_p$ at a fixed windsea Reynolds numbers, Re_B, equal to 4000, corresponding to the first appearance of bag breakup (solid curve) and 8000 (dashed curve).

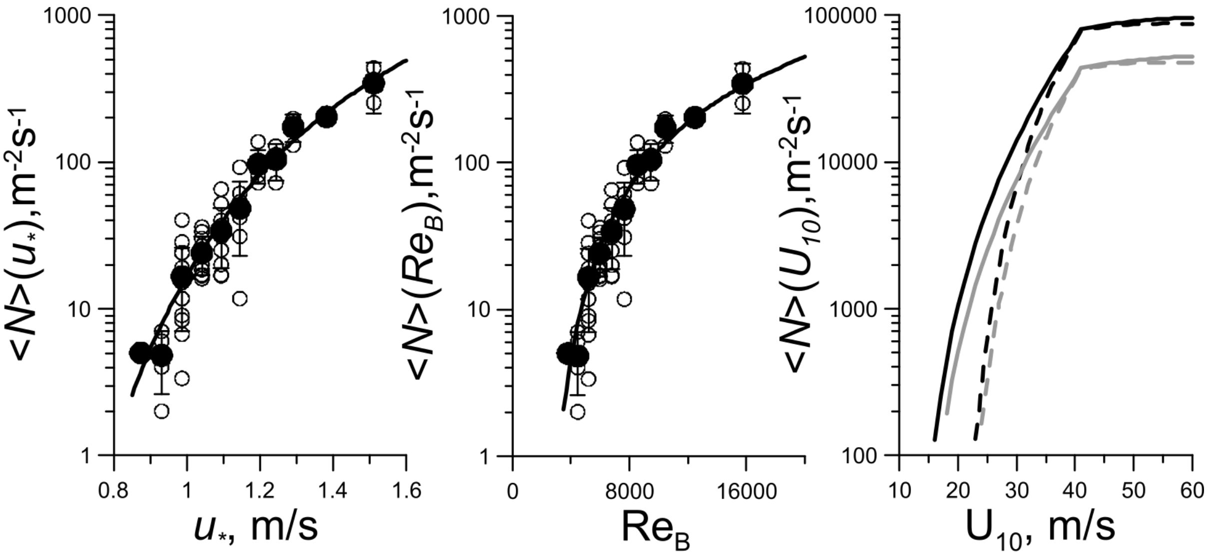

(a) (b) (c)

Fig. 9. Approximation of the experimental dependence of specific number of bags on friction velocity (a) using Eq. (5) and (b) on the windsea Reynolds number using Eq.(7). Open symbols are data obtained by processing individual 33,000-frame records, and closed symbols are the averaged data; the error bars are defined by the standard deviation. (c) Estimated specific number of bags using field conditions versus U_{10} for the wave-age parameter Ω=2.5 (black curves) and Ω=3.5 (grey curves); solid curves - Eq. (7), dashed curves - Eq. (9).

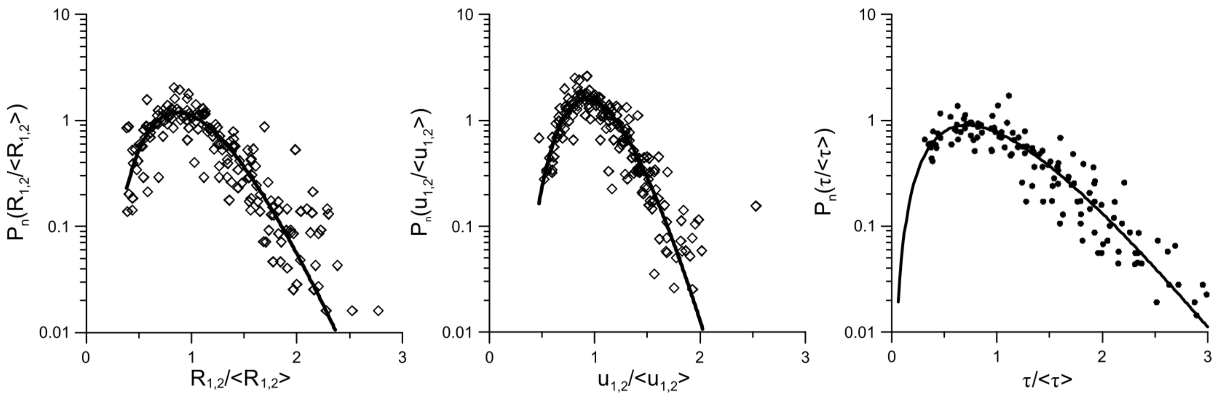

(a) (b) (c)

Fig. 10. (a) The frequency distribution of bag size at the moment of nucleation ($R_1/\langle R_1\rangle$ and at the moment of rupture ($R_2/\langle R_2\rangle$. (b) The frequency distribution of the velocity of the motion of bag edges ($u_1/\langle u_1\rangle$ and centers ($u_2/\langle u_2\rangle$. (c) The frequency distribution of bag lifetime ($\tau/\langle\tau\rangle$. Curves are the Gamma distribution for (a) n = 7.53, (b) n = 13.30, and (c) n = 3.70.

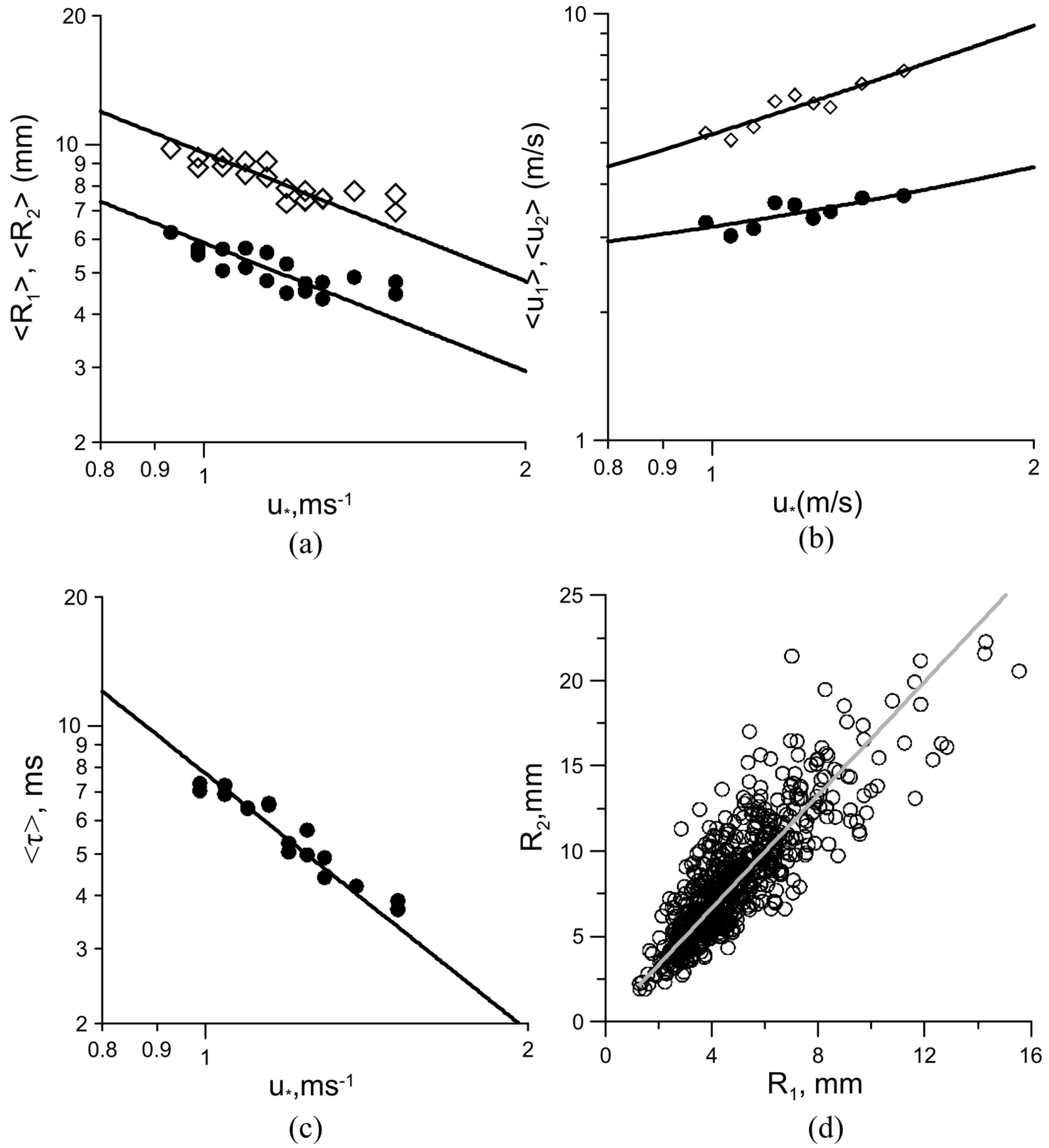

Fig. 11. Dependencies of averaged values on the friction velocity of the air flow: (a) the initial (closed circles) and final size (open diamonds) of bags, (b) the velocity of the edges (closed circles) and centers (open diamonds) of bags, and (c) the lifetime of bags. Lines are the power best fit from Eqs. (11-15). (d) Proportionality in the sizes of bags.

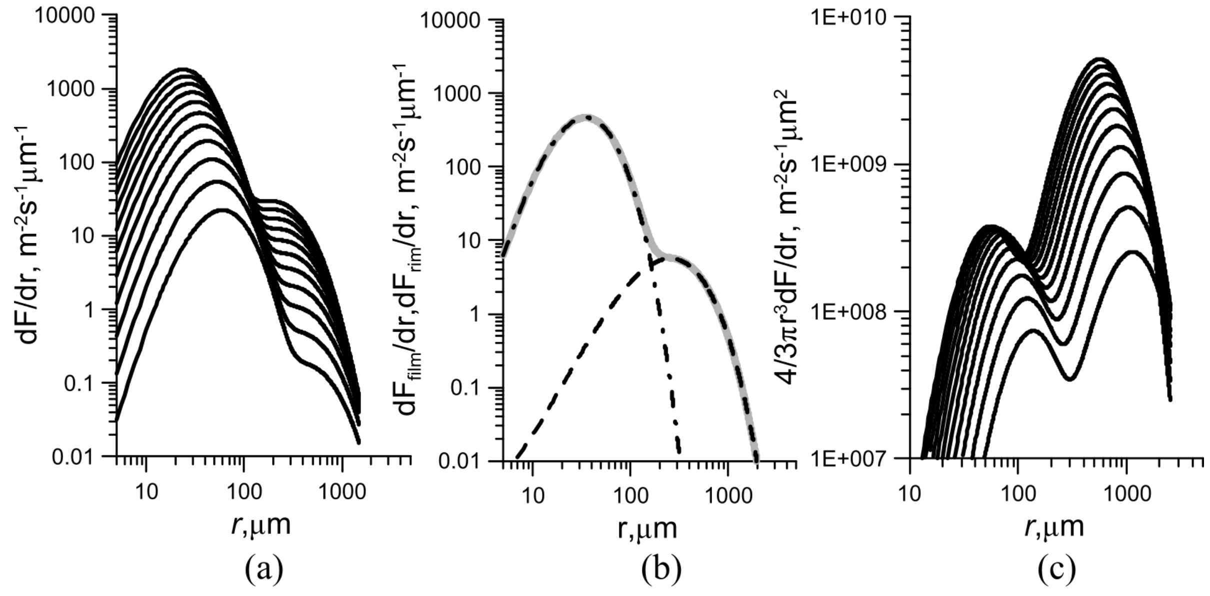

Fig. 12. (a) The bag breakup SGF. (b) The SGFs for the canopy (dash-dot curve) and rim (dashed curve) droplets and their aggregate (gray solid curve) for u_*=1.5 m/s. (c) Bag breakup SGF as the volume flux. For (a) and (c), u_* varies from 1 m/s to 2 m/s with an increment 0.1 m/s.

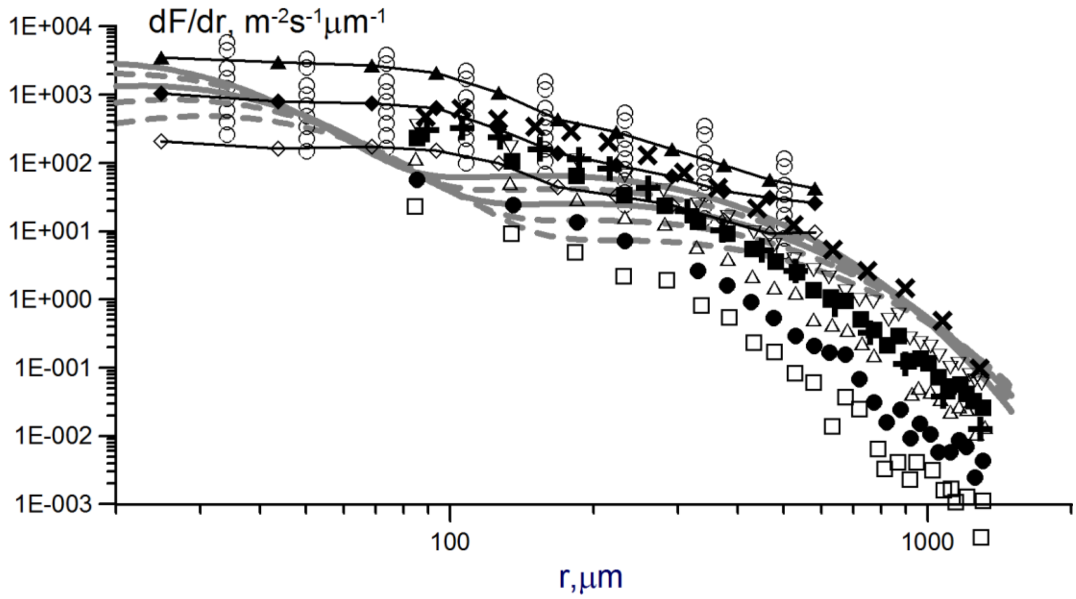

Fig. 13. Comparison of the bag breakup SGF (solid and dashed lines) with empirical estimations of SGFs under laboratory conditions. Symbols: Iida et al. (1992) - open circles; Ortiz-Suslow et al. (2016) - open squares - u_*=1.75 m/s (U_{10}=36 m/s), closed circles - u_*=1.97 m/s (U_{10}=40.5 m/s), upward-pointing triangles - u_*=2.19 m/s (U_{10}=45 m/s), closed squares - u_*=2.43 m/s (U_{10}=49.5 m/s), downward-pointing triangles - u_*=2.66 m/s (U_{10}=54 m/s); Veron et al. (2012) - crosses - u_*=1.98 m/s (U_{10}=41.2 m/s), X - u_*= 2.33 m/s (U_{10}=47.1 m/s). Fairall et al. (2009) - thin lines with symbols: open diamonds u_*= 1.35 m/s, closed diamonds u_*= 1.44 m/s, closed triangles u_*= 1.64 m/s. For the bag breakup SGF, u_* varies between 1.6 m/s and 2.4 m/s with an increment of 0.2 m/s. Solid lines correspond to u_*=2 m/s (lower) and u_*=2.4 m/s (upper).

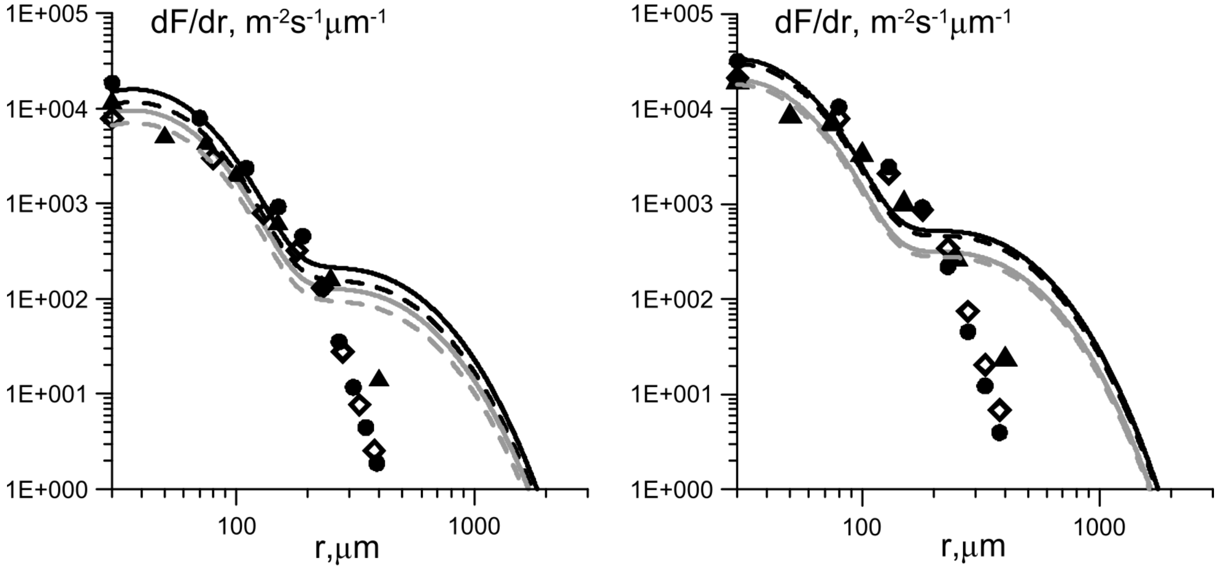

(a) (b)

Fig. 14. Comparison of the bag breakup SGF with empirical SGFs under field conditions by Andreas (1998) (diamonds), Fairall et al. (1994) (triangles), Zhao et al. (2006) (circles) at U_{10}=30 m/s (a) and U_{10}=35 m/s (b). In the bag breakup SGF, the wave-age parameter Ω=2.5 (black curves) and Ω=3.5 (grey curves); solid curves - Eq.(7), dashed curves - Eq. (9).